



Dynamic Cracking Behaviors and Energy Evolution of Multi-flawed Rocks Under Static Pre-compression

Zelin Yan¹ · Feng Dai¹ · Jianbo Zhu² · Yuan Xu³

Received: 19 September 2020 / Accepted: 24 June 2021 / Published online: 6 July 2021
© The Author(s), under exclusive licence to Springer-Verlag GmbH Austria, part of Springer Nature 2021

Abstract

Understanding the dynamic cracking behaviors and energy evolution of flawed rocks is highly relevant to underground rock engineering. In this study, multi-flawed rock specimens are tested under coupled static–dynamic compression using a modified SHPB system combined with high-speed photography and DIC monitoring. We systematically investigated the influences of pre-stress ratio, flaw inclination angle and strain rate on the dynamic progressive cracking mechanism and energy evolution of multi-flawed rocks. Experimental results show that the dynamic/total strength generally increases with increasing strain rate, featuring evident rate-dependence. With increasing flaw inclination angle from 15° to 60°, the dynamic/total strength initially decreases and subsequently increases with the minimum achieved around 45°. With the pre-stress ratio increasing from 0.2 to 0.8, the dynamic strength persistently decreases while the total strength initially increases and subsequently decreases with the maximum achieved at 0.6. Furthermore, based on the displacement trend lines method, a novel crack classification method is developed to analyze the progressive cracking mechanism of multi-flawed rocks using high-speed photography and DIC technique. Generally, mixed cracking dominates the failure of multi-flawed rocks under coupled static–dynamic compression. With increasing flaw inclination angle from 15°–60°, the predominant cracking mechanism changes from mixed tensile-shear cracking to mixed compression-shear cracking. The increasing pre-stress ratio promotes shear cracking under lower flaw inclination angles while facilitates tensile cracking under higher flaw inclination angles. In addition, the energy evolution for coupled static–dynamic SHPB tests is re-evaluated and a new energy calculation formula is proposed. The results show that the increasing strain rate reduces the energy utilization while promotes the energy dissipation density. Both the energy utilization and energy dissipation density increase with increasing pre-stress ratios.

Keywords Multi-flawed rocks · Coupled static–dynamic compression · SHPB · DIC · Cracking mechanism · Energy dissipation

1 Introduction

Due to the long-term geological movement and external effects, plenty of flaws including fissures, voids and discontinuities are widespread in natural rocks, which evidently weaken the stability of rock structures (Li et al. 2020a, b; Jiang et al. 2021). In underground rock engineering, flawed rocks are initially subjected to static tectonic stress or gravity stress and then dynamic loadings (e.g., drilling, blasting and seismic) (Xie et al. 2020; Zhang and Zhao 2014; Xia and Yao 2015). The underground rock structures are in a state of coupled static–dynamic combined loading, such as the rock pillars shown in Fig. 1. Thus, understanding the dynamic cracking behaviors and energy dissipation of flawed rocks under coupled static–dynamic compression loads is of high

✉ Feng Dai
fengdai@scu.edu.cn

¹ State Key Laboratory of Hydraulics and Mountain River Engineering, College of Water Resource and Hydropower, Sichuan University, Chengdu 610065, Sichuan, China

² Guangdong Provincial Key Laboratory of Deep Earth Sciences and Geothermal Energy Exploitation and Utilization, College of Civil and Transportation Engineering, Institute of Deep Earth Sciences and Green Energy, Shenzhen University, Shenzhen, China

³ Department of Engineering Science, University of Oxford, Oxford OX5 1PF, UK

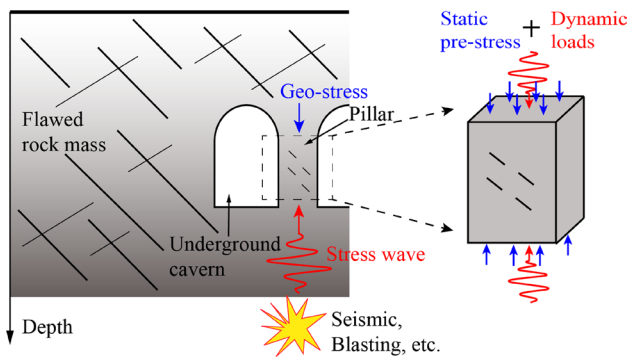


Fig. 1 Schematic of multi-flawed rocks subjected to coupled static–dynamic compression in underground rock engineering

relevance to the disaster mitigation and construction safety in rock engineering.

To date, majority of researches on the cracking behaviors and mechanical properties of flawed rocks are concentrated on pure static or dynamic loading conditions. Many uniaxial compression tests have been conducted on flawed rock specimens under quasi-static loading condition (Park and Bobet 2010; Prudencio and Sint 2007; Wong and Chau 1998; Yan et al. 2019), and their results indicate that the mechanical properties of flawed rocks are markedly affected by the flaw geometry (Liu et al. 2017; Zhou et al. 2019), especially the inclination angle of flaws (Huang et al. 2016). In addition, the progressive cracking behaviors of flawed rocks have also been widely investigated in quasi-static compression tests (Brace and Bombolakis 1963; Park and Bobet 2010; Zhang and Wong 2013a). They identified the nature of cracks into tensile wing cracks and secondary shear cracks. And researchers also have proposed many crack classification schemes (Bobet 2000; Bobet and Einstein 1998; Sagong and Bobet 2002; Shen 1995; Wong and Chau 1998). To eliminate some confusion, Wong and Einstein (2009a, b) further summarized previous studies and proposed seven crack types. Recently, some researchers investigated the failure modes of multi-flawed rocks under quasi-static compression loading (Bahaaddini et al. 2013; Lee and Jeon 2011). Four different failure types (i.e., shear failure, mixed failure, intact failure and stepped path failure) were identified by Cao et al. (2016). The split Hopkinson pressure bar (SHPB) has been widely utilized to measure the dynamic mechanical properties of rocks following the recommendation by the International Society for Rock Mechanics (ISRM). Recently, studies on the cracking behaviors and mechanical properties of flawed rocks are extended to dynamic loading conditions using the SHPB device (Li et al. 2017; Zhou et al. 2020a, b; Zou et al. 2016; Zou and Wong 2016). Their results indicate that the dynamic cracking behaviors and mechanical properties of flawed

rocks are quite different from that of under static loading condition. The cracking process of single-flawed marble was classified into two stages including the initiation of white patches and the development of macro-cracks (Zou and Wong 2014). Their experiments also show that all the failure modes of single-flawed marble are “X” shaped shear failure. Recently, Li et al. (2019) performed dynamic compression experiments on double-flawed rocks and they classified nine crack coalescence types. Their results indicate that the energy absorption of rock specimen is evidently affected by the artificial flaws.

However, in underground rock engineering, the loads that applied on rock structures are usually the coupled static–dynamic compression loads rather than the simple dynamic or static compression loads. Understanding the dynamic energy evolution and cracking mechanism of rocks under coupled static–dynamic compression loads is undoubtedly of significance for practical rock engineering. Existing researches on the dynamic properties of rocks under coupled static–dynamic loads are mainly concentrated on intact rocks while rare investigations can be found on flawed rocks (Li et al. 2020a, b; Weng et al. 2018). Using the modified SHPB system, Li et al. (2008) conducted coupled static–dynamic compression tests on siltstone and their results indicate that the coupled total strength of rocks is evidently larger than the individual dynamic strength or static strength. Zhou et al. (2020a, b) further investigated the energy evolution and fragment characteristics of intact rock specimens under coupled static–dynamic compression and identified four failure patterns, including intact, rock burst, axial splitting, and pulverization. Recently, Du et al. (2020a, b) conducted tri-axial coupled static–dynamic SHPB tests on sandstone with different radial and axial confine pressures, their results show that the dynamic mechanical properties are significantly enhanced by the radial confinement and the axial pre-compression.

As an important research topic that closely related to the practical rock engineering, rare literatures can be found to investigate the dynamic cracking mechanism of flawed rocks under coupled static–dynamic compression. During the past decades, many experiments have been conducted to investigate the cracking behaviors and cracking mechanism of flawed rocks under quasi-static loading (Bobet and Einstein 1998; Sagong and Bobet 2002; Wong and Einstein 2009a, b) or dynamic loading condition (Li et al. 2017, 2019), and researchers have classified different crack types. These classifications are based on the observation of crack propagation path and morphology, more comprehensive and cogent crack type classification methods still need to be developed to explain the complex cracking mechanism of multi-flawed rocks under dynamic loading. In addition, existing studies on the energy evolution of rocks under coupled static–dynamic loadings are based on the energy analysis of traditional

SHPB tests. It is still questionable whether such classical SHPB energy calculation method is also applicable for the coupled static–dynamic SHPB tests.

Although our previous studies have explored the dynamic cracking behaviors of single-flawed rock specimens under impact loading (Yan et al. 2020), it is still failed to deeply interpret the cracking mechanism with solid mechanic evidence. In the present work, multi-flawed rock specimens are tested using the axial confined SHPB system. Combining the high-speed photography with the digital image correlation (DIC) monitoring, a novel crack classification method is introduced to give new sights on the progressive cracking mechanism of multi-flawed rocks. In addition, based on the re-evaluation of the energy calculation formula for coupled static–dynamic SHPB tests, energy evolution characteristics of multi-flawed rocks are comprehensively investigated. The rest of this paper is organized as follows. Section 2 first introduces the specimen preparation and testing devices and then re-evaluates the energy calculation method for coupled static–dynamic SHPB tests. The experimental results are systematically reported in Sect. 3, including dynamic stress equilibrium, dynamic strength, progressive cracking behaviors and energy evolution. Section 4 comprehensively discusses two important issues regarding the novel crack classification method and the new energy calculation method. Section 5 summarizes the whole study and drawn the main conclusions.

2 Methodology

2.1 Specimen Preparation and Testing Scheme

In this study, Neijiang sandstone is used for our experiments (Xu and Dai 2018). All the rock specimens are cut from a homogeneous sandstone block along an identical direction. The multi-flawed rock specimens are prepared by a rigorous procedure. First, cuboid specimens are cut with a nominal size of $35 \times 35 \times 45 \text{ mm}^3$. Then, diamond saw is used to cut the flaws with an aperture of 1 mm and different inclination angles β (the angle between horizontal direction and flaw orientation as shown in Fig. 2a). Finally, the surface roughness of the multi-flawed rock specimens is polished to less than 0.02 mm. The flaw length and flaw spacing are fixed at 7 mm and 8 mm. Figure 2 shows the prepared rock specimens.

The ratio of axial pre-stress that applied on rock specimen to the unconfined compression strength (UCS) of the multi-flawed rock specimen is defined as the pre-stress ratio (k_{pre}) in this study. The testing scheme of this work consists of two groups. For the group A, with the pre-stress ratio fixed at 0.4, multi-flawed rock specimens with different inclination angles (15° , 30° , 45° and 60°) are tested under a wide range of loading rates. For the group B, with a fixed loading rate, the multi-flawed rock specimens are tested under distinct pre-stress ratios. Four different pre-stress ratios (i.e., 0.2, 0.4, 0.6 and 0.8) are considered in this study, referring to previous studies on intact rocks (Li et al. 2008; Zhou et al. 2020a, b). Using a MTS-793 rock testing system, unconfined compression tests are conducted to get the static strengths parameters of the multi-flawed rock specimens. Three specimens are tested for each flaw inclination angle and Table 1

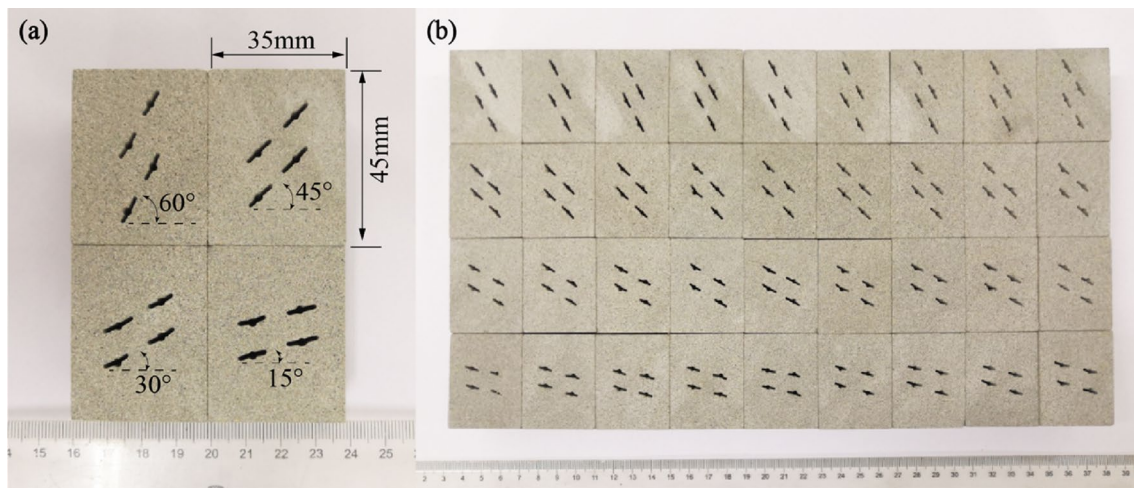


Fig. 2 a Illustration of the geometry of the multi-flawed rock specimens. b Part of the prepared specimens with different inclination angles

Table 1 Uniaxial compression strength of multi-flawed rock specimens with different inclination angles under quasi-static compression

Inclination angle	S1 (MPa)	S2 (MPa)	S3 (MPa)	Average (MPa)
15°	38.11	40.00	37.69	38.58
30°	36.39	39.11	39.60	38.36
45°	36.58	38.14	38.95	37.89
60°	39.01	38.43	40.02	39.15

lists the results. The average UCSs for the multi-flawed rock specimens with inclination angle of 15°, 30°, 45° and 60° are 38.58 MPa, 38.36 MPa, 37.89 MPa and 39.15 MPa, respectively.

2.2 Testing Apparatus and Procedure

A modified SHPB system is utilized to conduct the coupled static–dynamic compression tests on the multi-flawed rock specimens. This modified SHPB system is developed by adding the axial confinement unit to a traditional SHPB apparatus. The axial confinement unit mainly includes a hydraulic vessel, two rigid plate and four tie rods as noted in Fig. 3. The traditional SHPB device is generally composed of three bars including the striker bar, the incident bar and the transmitted bar. The diameter of the three bars

is 50 mm with lengths of 300 mm, 3000 mm and 2000 mm, respectively. The P-wave velocity and the density of bars are 5201 m/s and 7800 kg/m³, respectively. To eliminate the high frequency of oscillation of incident wave, the pulse shaping technique is essential in SHPB tests (Frew et al. 2002). In this study, the rectangular incident wave is shaped into a ramped wave by a small copper disk to promote the dynamic stress equilibrium of rock specimen.

During the experiments, the flawed rock specimen is firstly placed between the transmitted and incident bars. Note that the light high vacuum grease is used to lubricate both ends of rock specimen for minimizing the friction effects. After the successfully application of the axial pre-compression stress by the axial confinement unit, the striker bar is launched to first impact the pulse shaper and then the incident bar, yielding a non-dispersive incident wave. Upon arriving at the interface between incident bar and rock specimen, parts of the incident wave transmit through the rock specimen into the transmitted bar (i.e., transmitted wave), and the reflected parts are identified as the reflected wave. Strain gauges are separately mounted on the incident and the transmitted bars, and the three stress waves can be recorded.

For the coupled static–dynamic SHPB tests, the 1D stress wave propagation theory can be still guaranteed (Li et al. 2008). And the dynamic stress wave and the static pre-stress part meet the linear superposition (Xu et al. 2020). Because of the axial pre-compression, the baseline of the incident

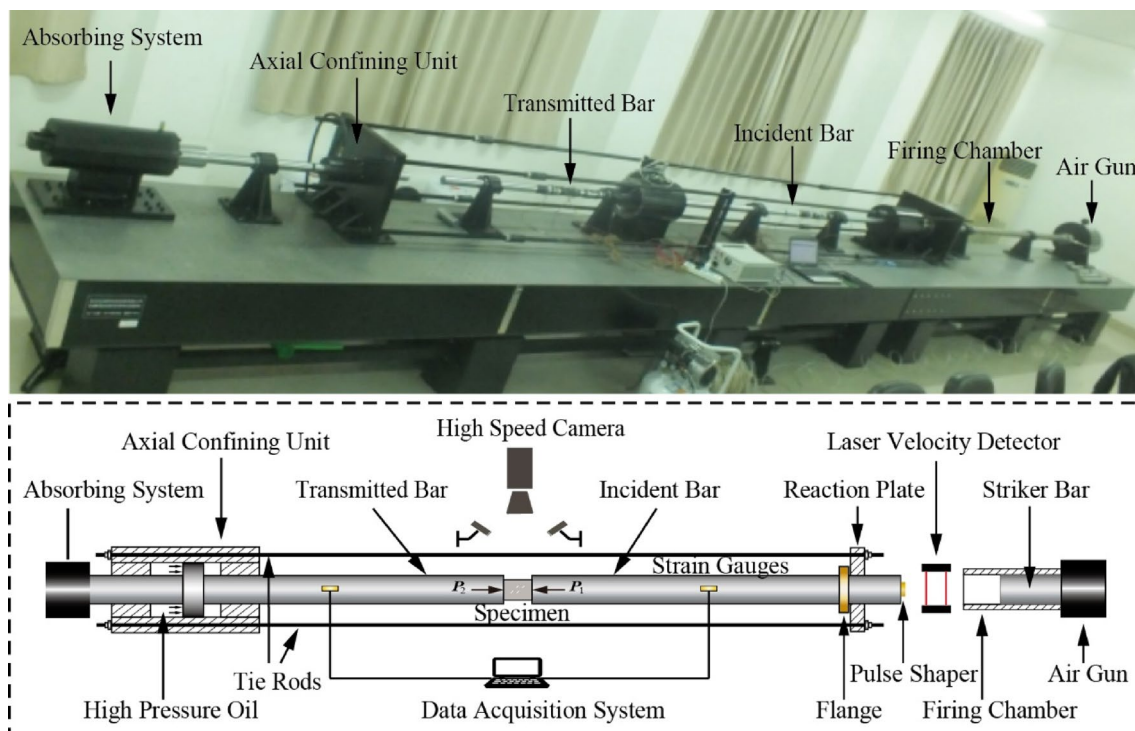


Fig. 3 Photograph and schematic of the SHPB system modified with an axial confinement unit

and transmitted wave is the static pre-stress (σ_{pre}). However, due to the existing of the detachment wave, the baseline of the reflected wave can be different (Chen et al. 2018). In our tests, calculations proved that the detachment wave reaches the strain gauges after the reflected wave have completely passed through the strain gauges. Thus, the baseline of the reflected wave is zero (Yan et al. 2020). The full strain signals (ϵ_{itotal} , ϵ_{rtotal} and ϵ_{ttotal}) containing the pre-strain (ϵ_{pre}) can be captured by the strain gauges. The dynamic stress histories on the specimen ends are determined by Eq. (1) based on 1D stress wave theory (Kolsky 1949). Upon the dynamic stress equilibrium prevails, Eq. (2) is commonly used to determine the dynamic stress (σ), strain (ϵ) and strain rate ($\dot{\epsilon}$) of rock specimens (Du et al. 2020b; Yan et al. 2020):

$$\begin{cases} P_1 = \frac{A_b}{A_s} E_b (\epsilon_{itotal} + \epsilon_{rtotal}) \\ P_2 = \frac{A_b}{A_s} E_b \epsilon_{ttotal} \end{cases}, \tag{1}$$

$$\begin{cases} \sigma(t) = \frac{A_b E_b}{A_s} (\epsilon_{ttotal} - \epsilon_{pre}) \\ \epsilon(t) = -\frac{2c_b}{L_s} \int_0^t \epsilon_{rtotal} dt \\ \dot{\epsilon}(t) = -\frac{2c_b}{L_s} \epsilon_{rtotal} \end{cases}, \tag{2}$$

where P_1 and P_2 are the dynamic stress history on both ends of specimen, respectively. A_b , E_b and c_b denote the cross-section area, elastic modulus and longitudinal wave velocity of the bar, respectively. A_s and L_s are the cross-section area and length of the specimen, respectively.

2.3 High-Speed Photography and Digital Image Correlation

The failure procedure of rock specimen under impact loading is very short in SHPB tests. Therefore, high-speed

photography is essential for capturing the whole cracking process of multi-flawed rock specimens. In this study, 180,000 fps with the resolution of 256×256 pixels is set for the high-speed camera. Two cold lights (600 W) were used to lighten the specimen surface. During the experiments, high-speed photography and the dynamic loading is strictly synchronized. Sequences of snapshots are captured covering the whole failure process of the multi-flawed rock specimens.

As an advanced non-contact optical measurement technology to monitor the deformation on specimen surface, the digital image correlation (DIC) technique has been extensively applied to investigate cracking behaviors of rocks under various loading conditions (Aliabadian et al. 2019; Sharafisafa et al. 2018; Xing et al. 2018). The fundamental principle of DIC technique is to track the position of the same pixels between a reference image and a sequence of deformed images using the correlation function (Pan 2018). The displacement of the center point of the subset is determined by matching the maximizing correlation coefficient as shown in Fig. 4a. The displacement of other pixels in the subset can be determined by Eq. (3):

$$\begin{cases} x'_i = x_i + u + u_x \Delta x + u_y \Delta y \\ y'_i = y_i + v + v_x \Delta x + v_y \Delta y \end{cases}, \tag{3}$$

where u and v are displacement component of the center point along the x - and y - direction, respectively; u_x , u_y , v_x and v_y are the first-order displacement gradient of the reference subset.

Repeating the algorithm for all subsets in the zone of interest (ZOI), the displacement field of tested specimen can be determined. Then, the strain field is obtained by differentiating the displacement field. Note that the result calculated by DIC is significantly influenced by the quality of speckle pattern. Commonly, a good speckle pattern has the following characteristics: high contrast, randomness, isotropy and stability (Pan et al. 2010). In our work, first, a thin matte white paint is sprayed on the surface of rock

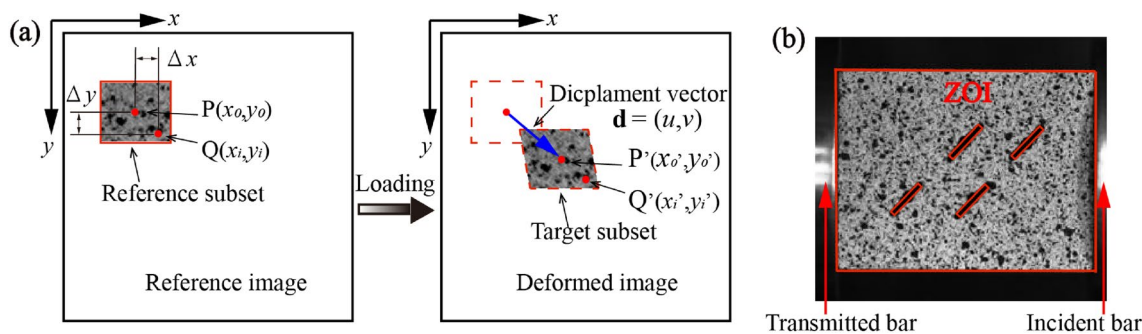


Fig. 4 a Schematic illustration of the principle of DIC algorithm; b typical multi-flawed specimen with speckle pattern and ZOI

specimen. After several hours, the white paint on the surface of rock specimen is completely dry. Then, the matte black paint is sprayed on the white surface to create random speckle pattern. This method has been widely adopted to generate random speckle patterns in good quality (Xing et al. 2018; Yan et al. 2020). Figure 4b shows a typical multi-flawed specimen with desired speckle pattern.

2.4 Energy Analysis for Coupled Static–Dynamic SHPB Tests

During the SHPB tests, the propagation of stress wave will produce both elastic deformation and motion of the bars (Song and Chen 2006). Therefore, the energy caused by stress waves consists of two parts, i.e., the elastic strain energy (U) and the kinetic energy (K). Since the propagation of stress waves is not affected by the axial pre-stress in coupled static–dynamic SHPB tests, the kinetic energy (K) is determined by particle velocity of the bars:

$$K = \iiint_V \frac{1}{2} \rho v^2 dV = \frac{1}{2} \int_0^t \rho (c_b \epsilon_d)^2 A_b c_b d\tau = \frac{c_b A_b E_b}{2} \int_0^t \epsilon_d^2 d\tau, \tag{4}$$

where c_b and ρ are the P-wave velocity and density of the bars. ϵ_d is the dynamic part of the strain signals.

Specifically, the kinetic energies caused by the incident wave (K_i), reflected wave (K_r) and transmitted wave (K_t) are determined by Eq. (5):

$$\begin{aligned} K_i &= \frac{c_b A_b E_b}{2} \int_0^t \epsilon_{id}^2 d\tau, \\ K_r &= \frac{c_b A_b E_b}{2} \int_0^t \epsilon_{rd}^2 d\tau, \\ K_t &= \frac{c_b A_b E_b}{2} \int_0^t \epsilon_{td}^2 d\tau. \end{aligned} \tag{5}$$

According to the elastic theory, the elastic strain energy in the bars can be determined by Eq. (6):

$$\begin{aligned} U &= \iiint_V \left(\int_{\epsilon_{pre}}^{\epsilon_{total}} E_b \epsilon d\epsilon \right) dV = \iiint_V \left(\frac{E_b}{2} (\epsilon_{total}^2 - \epsilon_{pre}^2) \right) dV \\ &= \frac{c_b A_b E_b}{2} \int_0^t (\epsilon_{total}^2 - \epsilon_{pre}^2) d\tau, \end{aligned} \tag{6}$$

where ϵ_{total} is the total strain of the bar, which is the sum of dynamic strain (ϵ_d) and pre-strain (ϵ_{pre}); ϵ_{pre} is the pre-strain of the bars induced by the axial pre-compression stress.

Specifically, elastic strain energies in the incident bar (U_i), reflected bar (U_r) and transmitted bar (U_t) can be determined by Eq. (7):

$$\begin{aligned} U_i &= \frac{c_b A_b E_b}{2} \int_0^t (\epsilon_{itotal}^2 - \epsilon_{pre}^2) d\tau, \\ U_r &= \frac{c_b A_b E_b}{2} \int_0^t (\epsilon_{rtotal}^2 - 0) d\tau, \\ U_t &= \frac{c_b A_b E_b}{2} \int_0^t (\epsilon_{ttotal}^2 - \epsilon_{pre}^2) d\tau. \end{aligned} \tag{7}$$

The total energy (W) is determined by the sum of kinetic energy (K) and elastic strain energy (U) by Eq. (8):

$$\begin{aligned} W_i &= K_i + U_i = c_b A_b E_b \int_0^t (\epsilon_{itotal}^2 - \epsilon_{itotal} \epsilon_{pre}) d\tau, \\ W_r &= K_r + U_r = c_b A_b E_b \int_0^t (\epsilon_{rtotal}^2) d\tau, \\ W_t &= K_t + U_t = c_b A_b E_b \int_0^t (\epsilon_{ttotal}^2 - \epsilon_{ttotal} \epsilon_{pre}) d\tau. \end{aligned} \tag{8}$$

Then, the energy absorbed by the rock specimen (W_a) is determined by Eq. (9):

$$W_a = W_i - W_r - W_t. \tag{9}$$

The energy utilization efficiency (k_w) is determined by the ratio of absorbed energy (W_a) of specimen to the incident energy (W_i):

$$k_w = W_a / W_i. \tag{10}$$

And the energy dissipation density (η_w) is determined by Eq. (11):

$$\eta_w = W_a / V, \tag{11}$$

where V denotes the specimen volume.

3 Experimental Results

3.1 Dynamic Stress Equilibrium

As a valid SHPB test, dynamic stress equilibrium of tested rock specimen shall be guaranteed before the further interpretation of experimental results. In this study, the rectangular incident wave is shaped into a non-dispersive ramped wave to promote the dynamic stress equilibrium of rock specimen (Dai et al. 2010). Based on the 1D stress wave theory, by shifting the three stress waves to the interface between bars and specimen, the dynamic stress histories on the specimen ends can be determined by Eq. (1). Figure 5 shows the dynamic stress equilibrium check in this study. At the beginning of the dynamic loading process, the reflected stress is zero, while the incident and transmitted wave equals to the axial pre-stress. After several reverberation of stress wave inside the rock specimen, dynamic stresses on

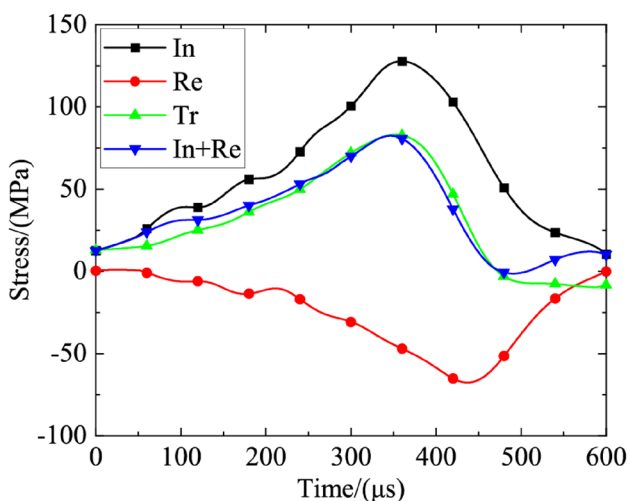


Fig. 5 Dynamic stress equilibrium check for multi-flawed rock specimen under coupled static-dynamic compression

specimen ends match with each other during the whole loading process. It is thus can be concluded that the multi-flawed rock specimen has achieved the dynamic stress equilibrium state in our experiments.

3.2 Dynamic Mechanical Properties

Once the rock specimen has achieved the dynamic stress equilibrium during the impact loading, the dynamic stress-strain curves can be derived by Eq. (2). Figure 6 presents the dynamic stress-strain curves of multi-flawed rock specimens with distinct inclination angles under a fixed pre-stress ratio of 0.4 (i.e., the test group A). It is worth noting that the static deformation parts induced by the axial pre-compression stress are not included in the dynamic stress-strain curves. All these stress-strain curves show similar characteristics. However, it can be seen that the strain rate significantly affects the dynamic mechanical properties: the failure strains generally increase with of increase of strain rate.

Table 2 lists the tested results of group A. The sum of dynamic strength and its corresponding axial pre-stress is

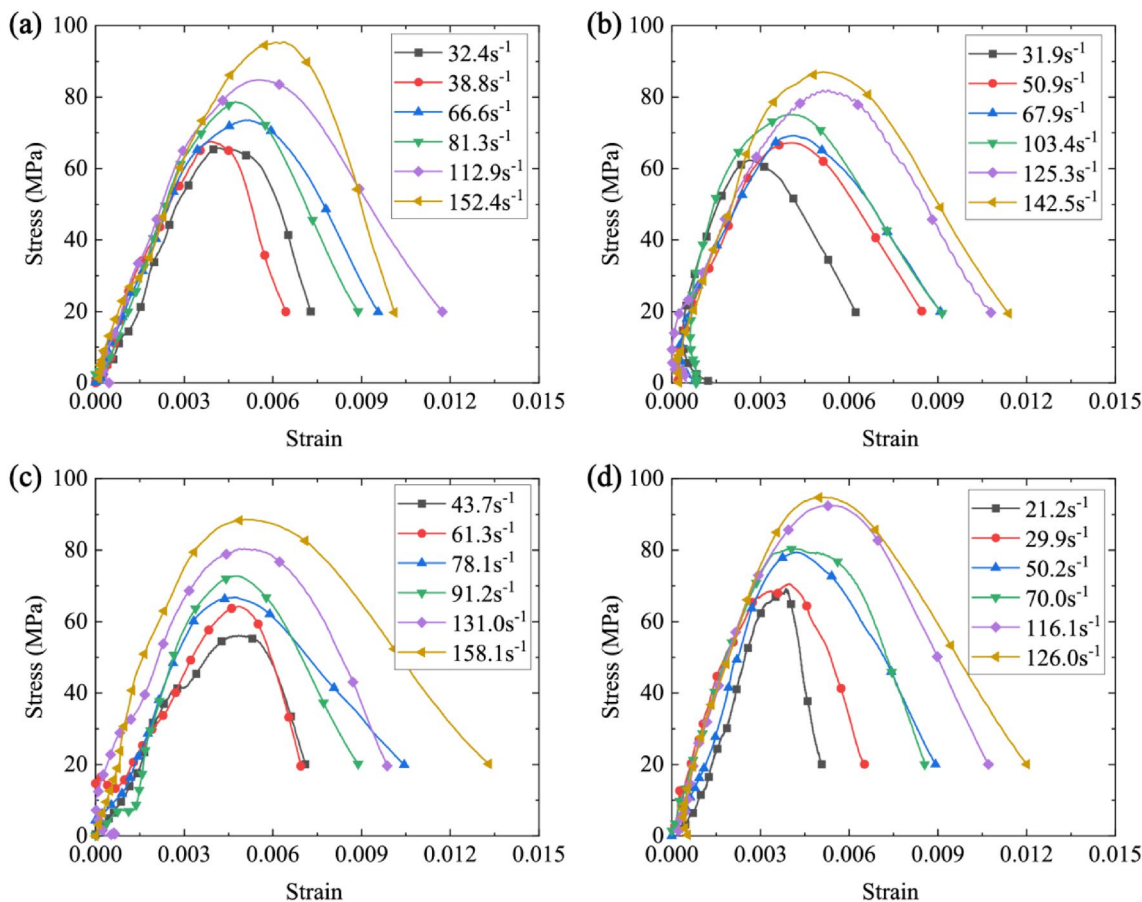


Fig. 6 Dynamic stress-strain curves of multi-flawed rock specimens with different inclination angles a 15°, b 30°, c 45°, d 60° under a fixed pre-stress ratio of 0.4

Table 2 Mechanical properties of multi-flawed rock specimens with different inclination angles under coupled static–dynamic compression with a fixed pre-stress ratio of 0.4

Specimen No	Pre-stress (MPa)	Inclination angle (°)	Strain rate (/s)	Dynamic strength (MPa)	Total strength (MPa)
A15-D4-1	15.4	15	32.4	65.5	81.2
A15-D4-3	15.4	15	38.8	67.4	83.0
A15-D4-5	15.4	15	66.6	73.3	89.0
A15-D4-4	15.4	15	81.3	78.5	94.1
A15-D4-6	15.4	15	112.9	84.6	100.2
A15-D4-2	15.4	15	152.4	95.2	110.8
A30-D4-3	15.3	30	31.9	62.5	77.7
A30-D4-1	15.3	30	50.9	67.4	82.5
A30-D4-4	15.3	30	67.9	69.4	84.5
A30-D4-5	15.3	30	103.4	75.3	90.5
A30-D4-6	15.3	30	125.3	82.1	97.3
A30-D4-2	15.3	30	142.5	87.2	102.4
A45-D4-3	15.1	45	43.7	57.9	73.3
A45-D4-1	15.1	45	61.3	64.1	79.4
A45-D4-2	15.1	45	78.0	66.6	81.9
A45-D4-5	15.1	45	91.2	72.6	87.9
A45-D4-6	15.1	45	131.0	80.2	95.6
A45-D4-4	15.1	45	158.1	88.4	103.7
A60-D4-6	15.7	60	21.1	69.5	84.9
A60-D4-1	15.7	60	29.9	70.8	86.3
A60-D4-3	15.7	60	50.2	79.7	95.1
A60-D4-4	15.7	60	70.0	80.8	96.2
A60-D4-5	15.7	60	116.1	92.7	108.1
A60-D4-2	15.7	60	126.0	95.0	110.5

defined as the total strength. It is evident that the dynamic/total strength is larger than the quasi-static strength. The influences of strain rate on the dynamic and total strength are shown in Fig. 7a, c, respectively. Obviously, the dynamic/total strength shows remarkable rate-dependence. Specifically, with increasing strain rate from ~30 to ~150/s, the dynamic strength increases from ~60 to ~90 MPa and the total strength increases from ~75 to ~105 MPa. Moreover, the influences of flaw inclination angle on the dynamic and total strength are shown in Fig. 7b, d. For a fixed loading rate, the dynamic/total strength initially decreases and subsequently increases with the flaw inclination angle increasing from 15° to 60°, among which the minimal values are achieved around 45°.

Figure 8 presents the complete stress–strain curves of multi-flawed rock specimens under different pre-stress ratios with approximate strain rates (i.e., the test group B). Note that the complete stress–strain curves are the combination of the dynamic stress–strain curves and quasi-static stress–strain curves. The initial points of the dynamic stress–strain curves correspond to the axial pre-stresses that applied to the rock specimens. It is evident that the dynamic part of the curves is quite different from the static part of the

curves. The dynamic deformation modulus of the curves is much larger than the quasi-static ones.

Table 3 lists the dynamic properties of tested rock specimens under different pre-stress ratios. Figure 9 shows the influences of pre-stress ratio and flaw inclination angle on the dynamic and total strength. For a fixed pre-stress ratio, the dynamic/total strength reaches the minimal values at flaw inclination angle of 45° and the maximal values at 60°. For a given flaw inclination angle, the dynamic strength monotonously decreases with increasing pre-stress ratios from 0.2 to 0.8. However, the total strength initially increases and subsequently decreases with the maximum values achieved at pre-stress ratio about 0.6. Similar results have been reported in previous studies (Li et al. 2008). They believed that the transition of total strength may be related to the exceeding of yield point of rock specimen under static pre-compression (Zhou et al. 2020a, b). Our study confirmed this viewpoint again as shown in Fig. 8, from which it can be found that the multi-flawed rock specimens have indeed entered the plastic yield stage in the quasi-static stress–strain curves under the pre-stress ratio of 0.8.

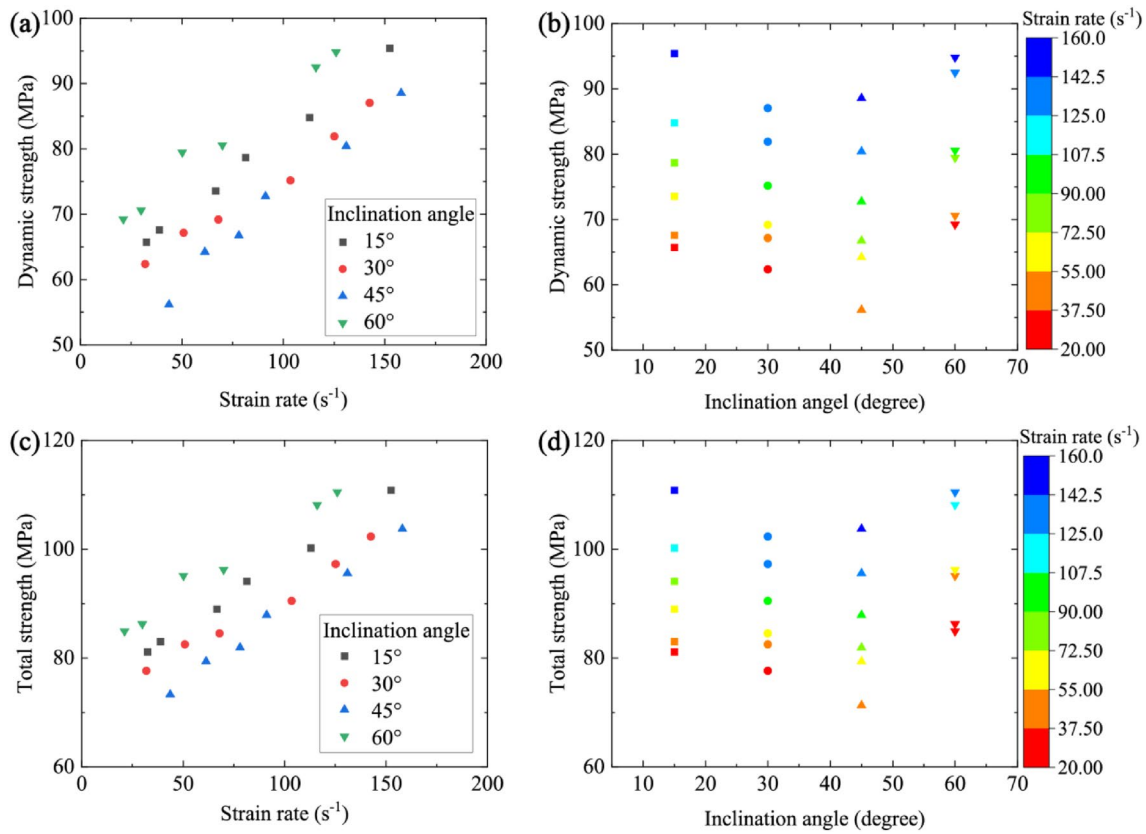


Fig. 7 Influences of strain rate and flaw inclination angle of flaws on the dynamic strength and total strength: **a** dynamic strength versus strain rate; **b** dynamic strength versus flaw inclination angle; **c** total strength versus strain rate; **d** total strength versus flaw inclination angle

3.3 Cracking Behaviors and Failure Modes

3.3.1 A Novel Crack Classification Method

Using the high-speed photography, progressive cracking processes of the multi-flawed rocks are captured. According to the DIC algorithm, the maximal principle strain field and the displacement field can be visualized to analyze the progressive cracking behaviors of multi-flawed rocks. Then, based on the displacement trend line (DTL) method, a novel crack type classification is proposed for further understanding of the progressive cracking mechanism of multi-flawed rocks under coupled static–dynamic compression.

The tested rock specimens will axially deform during the loading process. By matching the positions of the same pixel on the specimen surface before and after deformation using DIC technique, the displacement vector of each pixel can be obtained. If the displacement vectors of all pixels are plotted, the displacement field will be very dense and fuzzy, and even local amplification is not effective for cracking analysis. Therefore, the displacement vectors in a region of 14×18 pixel (around 2.748×3.534 mm) are averaged, so that the clear and effective displacement field can be illustrated for

cracking analysis. At the beginning of dynamic loading, the specimen does not deform and there are only some random tiny arrows as shown in Fig. 10a. As the loading continues, the rock specimen is uniformly compressed. And the displacement vectors are uniformly distributed towards the transmitted end of specimen as shown in Fig. 10b. When a crack initiates and propagates on the specimen surface, the displacement field in the area near the new developed crack would become discontinuous (Zhang and Wong 2014). In other words, the displacement vectors on both sides of the newly developed crack can be different in terms of magnitudes and directions as shown in Fig. 10c. To deeply understand the fracture mechanism of the newly developed crack, displacement trend lines (DTLs), which are schematically simplified by two bold blue arrows, are introduced to represent the general displacement trends near the both sides of the newly developed crack (Zhang and Wong 2014). Since the locations of DTLs significantly affect the cracking analysis, a quantitative standard is essential to determine the starting positions of DTLs. If the starting positions of DTLs are far away from the newly developed crack, the DTLs cannot reflect the cracking nature. On the contrary, if the starting positions are quite close to the new crack, the

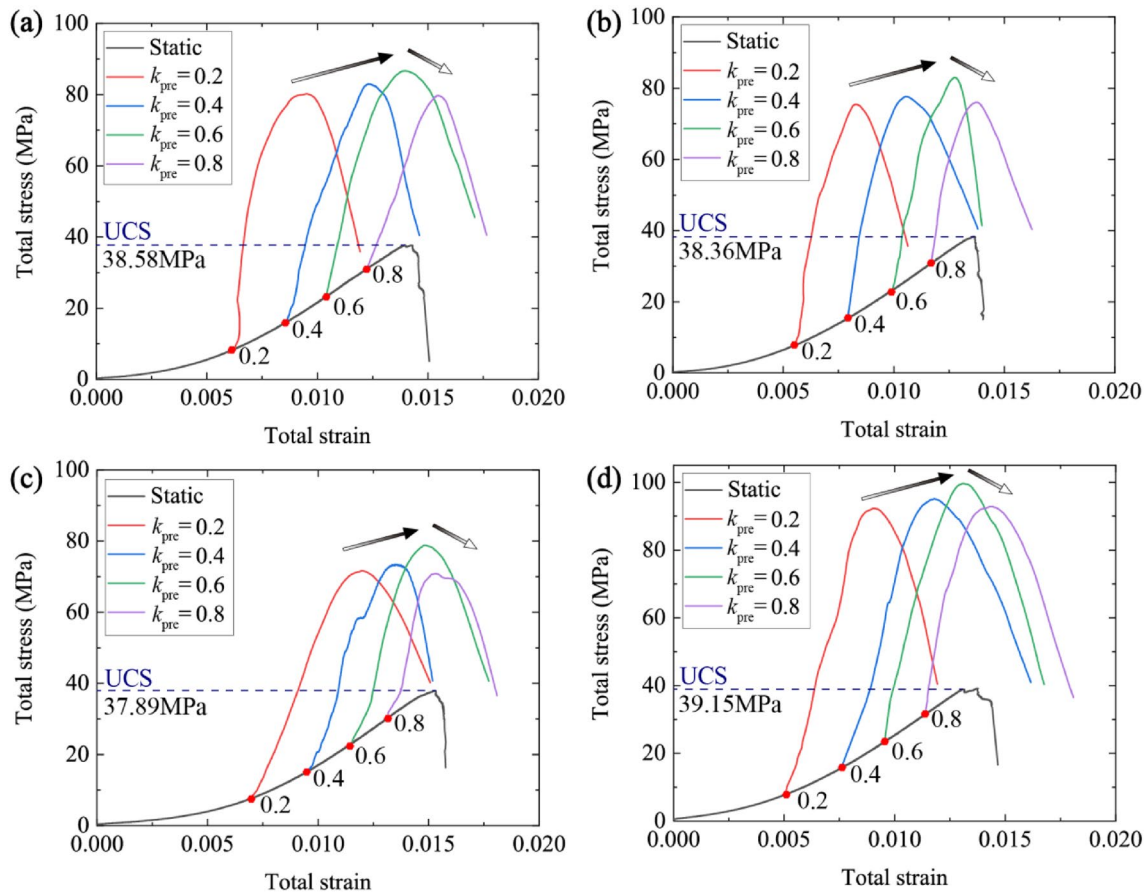


Fig. 8 Complete stress–strain curves of the multi-flawed rock specimens under different pre-stress ratio: **a** flaw inclination angle of 15°, **b** flaw inclination angle of 30°, **c** flaw inclination angle of 45°, **d** flaw inclination angle of 60°. The strain rate is fixed around 45/s

Table 3 Mechanical properties of multi-flawed rock specimens with different inclination angles under different pre-stress ratios with a fixed strain rate at ~45/s

Specimen No	Pre-stress (MPa)	Inclination angle (°)	Strain rate (/s)	Dynamic strength (MPa)	Total strength (MPa)
A15-D2-3	7.7	15	40.1	73.2	80.2
A15-D4-3	15.4	15	38.8	67.4	83.0
A15-D6-3	23.1	15	44.1	63.5	86.7
A15-D8-3	30.9	15	45.6	48.6	79.7
A30-D2-3	7.6	30	36.3	67.8	77.2
A30-D4-3	15.3	30	31.9	62.5	77.7
A30-D6-3	23.0	30	44.1	58.9	83.1
A30-D8-3	30.6	30	38.3	45.1	76.1
A45-D2-3	7.5	45	44.3	64.0	71.7
A45-D4-3	15.1	45	43.7	57.9	73.3
A45-D6-3	22.7	45	66.8	56.1	78.8
A45-D8-3	30.3	45	26.4	39.5	67.8
A60-D2-3	7.8	60	44.1	84.2	94.2
A60-D4-3	15.7	60	50.2	79.7	95.1
A60-D6-3	23.9	60	47.7	76.2	99.7
A60-D8-3	31.3	60	53.2	61.5	92.9

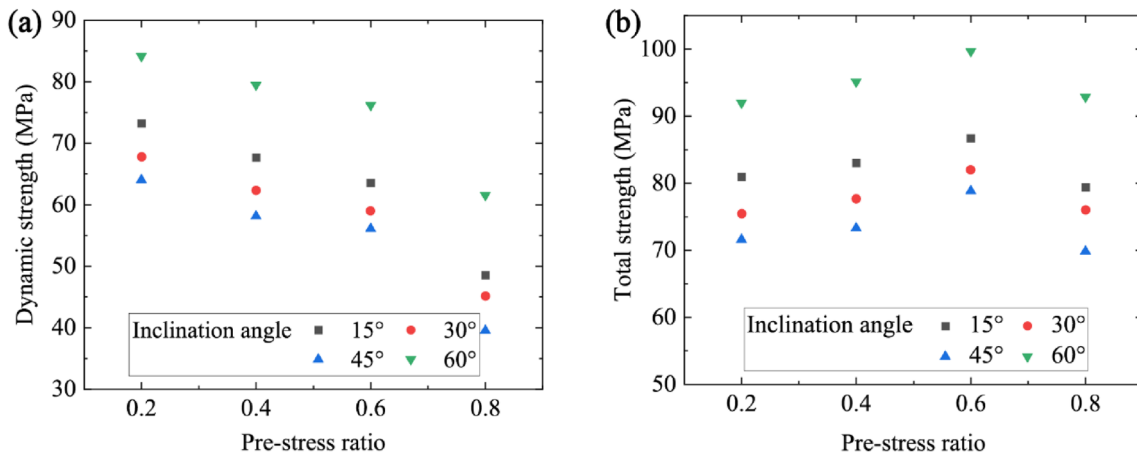
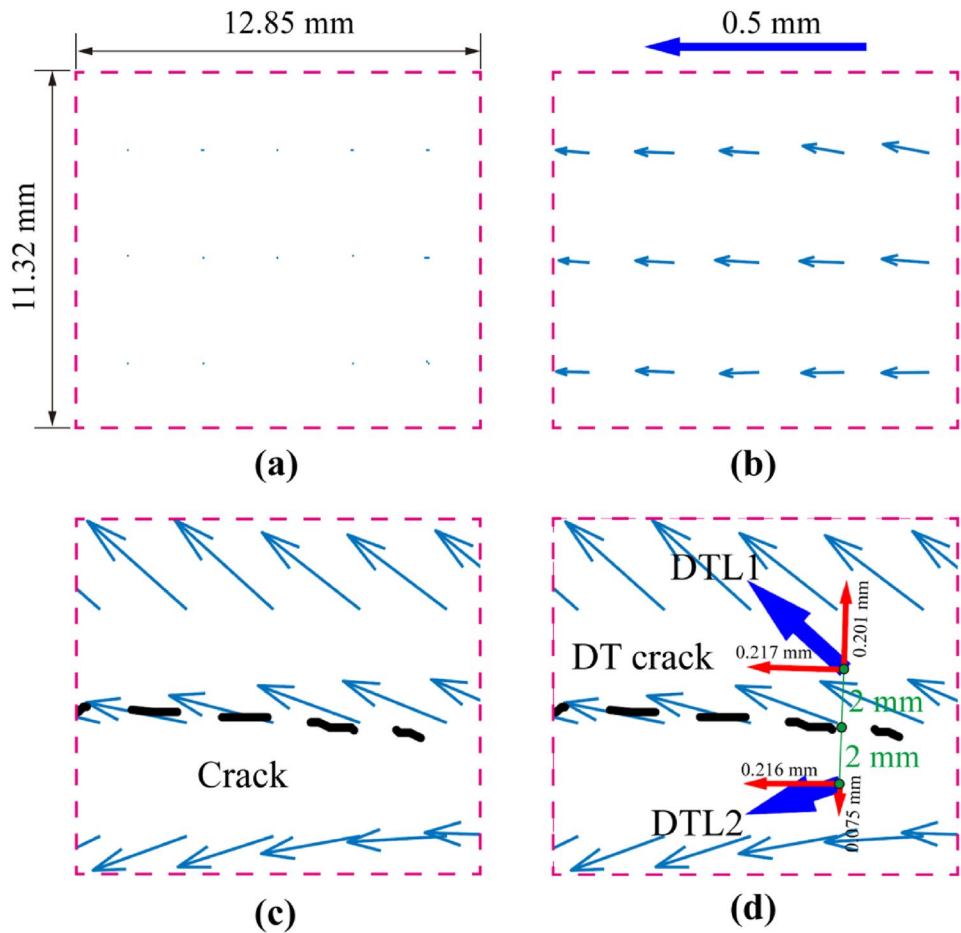


Fig. 9 Influences of pre-stress ratio and the flaw inclination angle on the dynamic strength and total strength: **a** dynamic strength versus pre-stress ratio; and **b** total strength versus pre-stress ratio

Fig. 10 Illustration of the displacement trend lines method: **a** initial state; **b** a uniform and continuous displacement field; **c** displacement vectors varied abruptly in the vicinity of a newly developed crack (black dash line); **d** DTLs (blue arrows) on both sides of the crack and its component vectors (red arrows)



large displacement or discontinuous deformation near the newly developed crack can result in substantial measurement errors (Ji et al. 2016). According to previous studies (Lin et al. 2014, 2020; Ji et al. 2016) on the rock fracture behaviors using DIC, the distance between the starting positions

of DTLs and crack is set about ten times the size of a pixel point. Since the magnification factor $M=0.1963$ mm/pixel in the experiments, the distance between the starting point of DTL and the crack is determined as 2 mm as show in Fig. 10d. Then, the two DTLs are decomposed along the

direction parallel and perpendicular to the newly developed crack. Since the DTL vectors are determined by the displacement vectors via DIC, the exact magnitude and orientation of the parallel/perpendicular components can also be exactly determined by the triangular geometry relationship. By comparing the direction and magnitude of the two perpendicular component vectors, tensile properties of the newly developed crack can be identified. Similarly, by comparing the direction and magnitude of the two parallel component vectors, shear properties of the newly developed crack can be identified. Based on the identification principle stated above, eight crack types can be identified as shown in Fig. 11, and the basis of the crack classification are detailed below:

Type I (Fig. 11a): the parallel component vectors have the same magnitude and directions, while the perpendicular component vectors have the opposite directions. This type of crack is identified as direct tensile crack, denoted as DT crack.

Type II (Fig. 11b): the parallel component vectors have the same magnitude and directions, while the perpendicular component vectors have the same direction but different magnitudes. This type of crack is identified as relative tensile crack, denoted as RT crack.

Type III (Fig. 11c): the perpendicular component vectors have the same magnitude and directions, while the parallel component vectors have the opposite directions. This type of crack is identified as direct shear crack, denoted as DS crack.

Type IV (Fig. 11d): the perpendicular component vectors have the same magnitude and directions. The parallel component vectors have the same direction, while their magnitudes are significantly different. This type of crack is identified as relative shear crack, denoted as RS crack.

Type V (Fig. 11e): the perpendicular component vectors have the opposite directions, and the parallel component vectors also have the opposite directions. This type of crack is identified as tensile-shear mixed crack, denoted as TS1 crack.

Type VI (Fig. 11f): the perpendicular component vectors have the opposite directions. The parallel component vectors have the same direction, while their magnitudes are significantly different. This type of crack is also identified as tensile-shear mixed crack, denoted as TS2 crack.

Type VII (Fig. 11g): the perpendicular component vectors have the same direction, while their magnitudes are significantly different. The parallel component vectors have the opposite directions. This type of crack is identified as compression-shear mixed crack, denoted as CS1 crack.

Type VIII (Fig. 11h): the perpendicular component vectors have the same direction, while their magnitudes are significantly different. The parallel component vectors have the same direction, while their magnitudes are also significantly different. This type of crack is also identified as compression-shear mixed crack, denoted as CS2 crack.

Among the above eight crack types, the first four crack types (i.e., type I–IV) are the basic cracks, and the last four crack types (i.e., type V–VIII) are mixed cracks. Note that the magnitudes of the components two pairs of DTLs rarely have the exact same values. If the relative difference of a pair of DTL components is smaller than 1%, they are believed to have the “same magnitudes”.

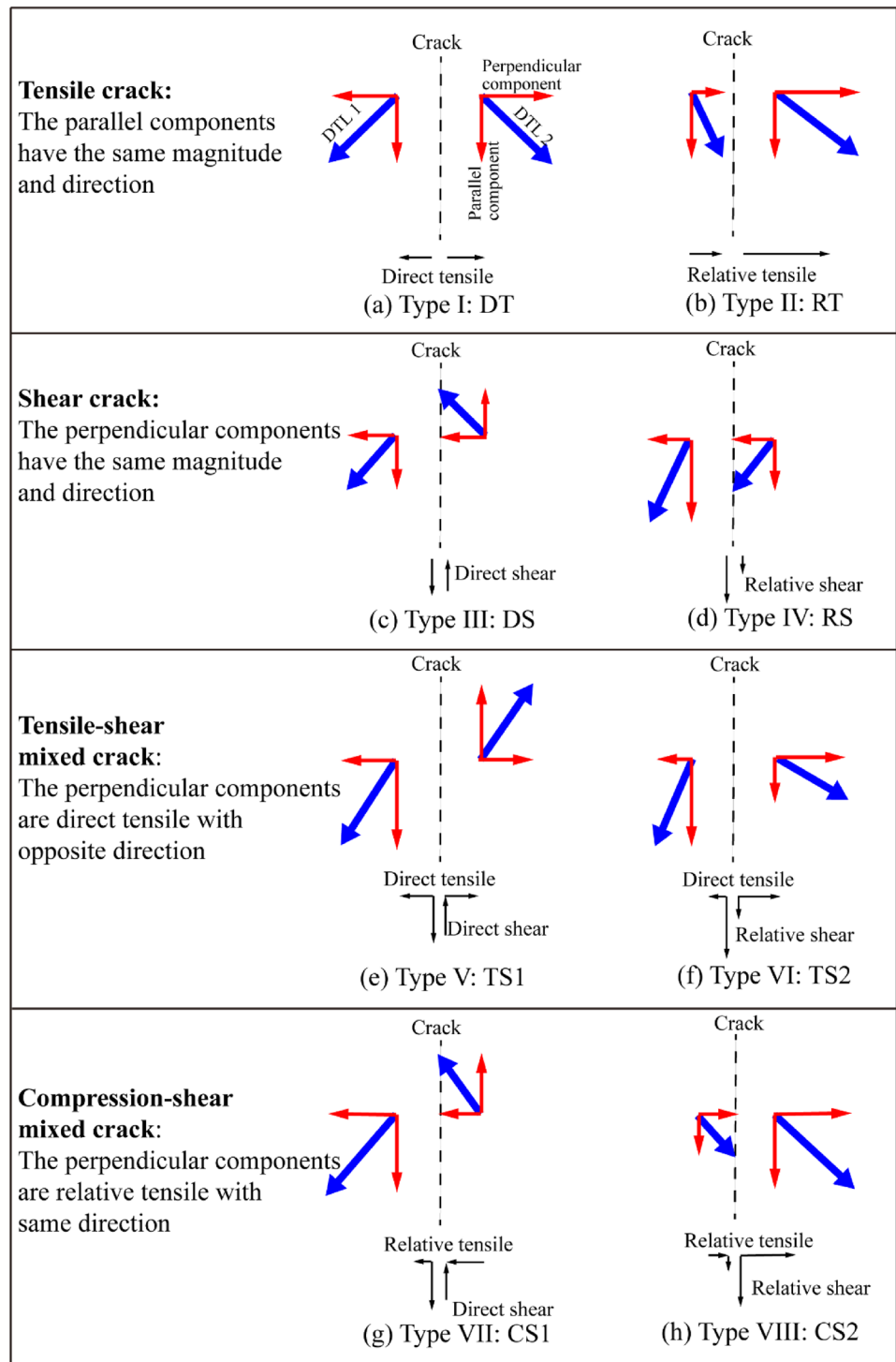
3.3.2 Progressive Cracking Behaviors

In this section, four typical multi-flawed rock specimens with different inclination angles are selected to investigate the progressive cracking behaviors under coupled static–dynamic compression. The progressive failure photographs and their corresponding maximal principle strain field and displacement field are shown in Fig. 12. For each specimen, five snapshots are selected covering the initial stage, fracture initiation and propagation process, peak stress and the post-peak failure. To illustrate the fracture mechanism of some local cracks more clearly, three typical crack types are highlighted in each diagram. For each photograph, the left and right sides of the tested specimen are the transmitted bar and incident bar, respectively.

Figure 12a presents the typical progressive cracking behaviors of multi-flawed rock specimen with inclination angle of 15° . The first frame corresponds to the moment when the rock specimen started to be loaded ($0 \mu\text{s}$). The strain field and displacement field indicate that there is no deformation on the rock specimen at this moment. As the loading continues, the rock specimen is uniformly compressed for a long period. Due to high strain concentration, a CS2 crack emanates from the outer tip of flaw at $288.9 \mu\text{s}$. After that, a direct tensile crack (DT crack) emanates from the inner flaw tip at $305.6 \mu\text{s}$. Then, the rock specimen reaches the peaks stress at $327.8 \mu\text{s}$, and a TS2 crack emanates from the outer tip of flaw to connect with the specimen end. During the post-peak stage ($377.8 \mu\text{s}$), a tensile crack (DT crack) appears near the incident end of rock specimen and coalesce with existing flaws.

Figure 12b presents the progressive cracking behaviors of multi-flawed rock specimen with inclination angle of 30° . At the moment of $288.9 \mu\text{s}$, strain concentration occurs at the inner tips of flaws and the corner of specimen, and a TS2 crack emanates from the inner tip of flaw. As the loading continues, more cracks (i.e., RT crack, CS2 crack, TS2 crack and CS2 crack) start to emanate from other flaw tips at $322.2 \mu\text{s}$. The strain concentrations near the newly developed cracks are significantly intensified. After that, the rock specimen reaches the peak stress at $350 \mu\text{s}$, and the existing cracks further propagate. With the specimen stress gradually dropping down during the post-peak stage ($383.3 \mu\text{s}$), some tensile cracks (i.e., DT crack and RT crack)

Fig. 11 Eight crack types defined by DTLs method. (The dash lines represent the newly developed cracks. The bold blue arrows are the DTLs. The red arrows are the component vectors decomposed by the DTLs along the directions perpendicular and parallel to the crack)



also originate from the incident end of rock specimen and propagate horizontally.

Figure 12c presents the typical progressive cracking behaviors of multi-flawed rock specimen with inclination angle of 45°. When the rock specimen is loaded to 277.8 μs , symmetrical strain concentrations appear near the flaw tips and a TS2 crack originates from the inner tips of flaws. As

the loading continues, a pair of symmetrical DT cracks emanate from the outer tips of flaws at 305.6 μs . When the rock specimen is loaded to reach the peak stress (327.8 μs), mixed cracks (TS2 crack and CS2 crack) propagate towards the specimen ends accompanied with evident strain concentration. Then, the specimen stress decreases dramatically during the post-peak stage and more compression-shear

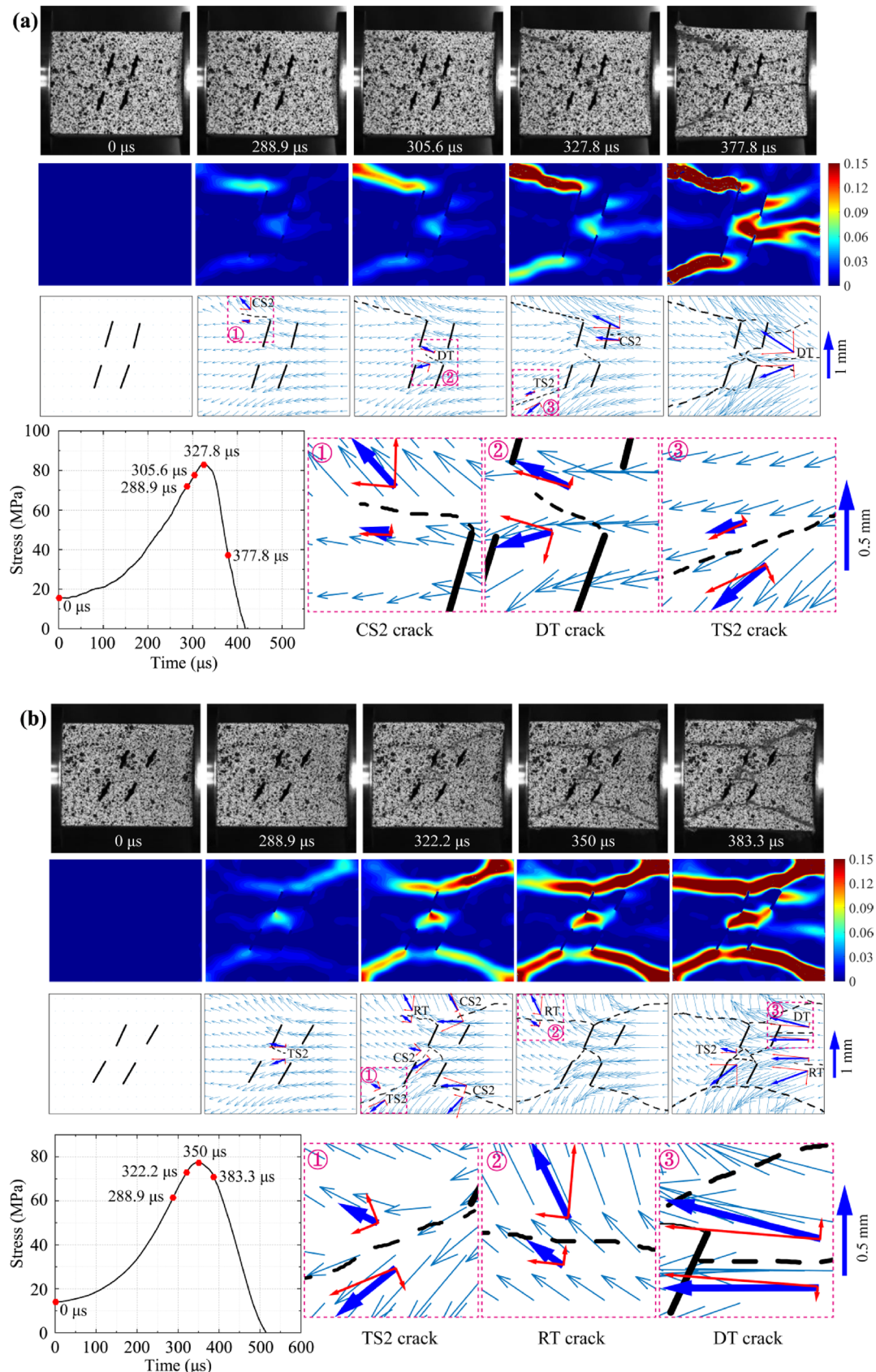


Fig. 12 Influence of flaw inclination angle on the progressive failure behaviors of flawed rock specimens under coupled static–dynamic compression: **a** flaw inclination angle of 15°, **b** flaw inclination angle of 30°, **c** flaw inclination angle of 45°, **d** flaw inclination angle of 60°. The pre-stress ratios are fixed at 0.4 and the strain rate is fixed at ~45/s

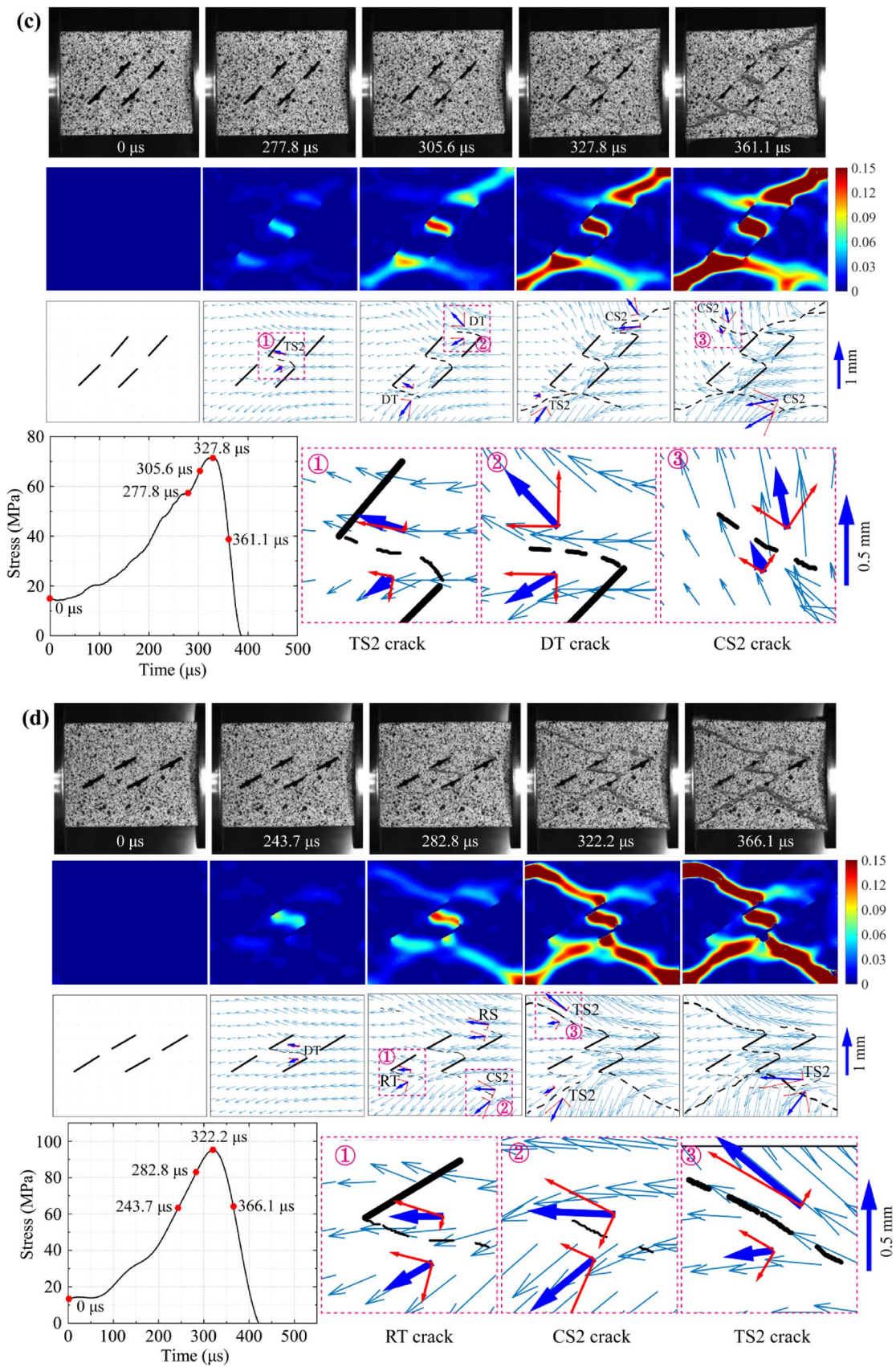


Fig. 12 (continued)

mixed cracks (CS2 crack) propagate to the specimen ends (361.1 μs).

Figure 12d presents the typical progressive cracking behaviors of multi-flawed rock specimen with inclination angle of 60° . At 243.7 μs , strain concentration occurs at the inner tips of flaws and then the inner tips of flaws are connected by a DT crack. After that, strain concentration is symmetrically intensified at flaw tips and specimen ends, and more cracks (RT crack and RS crack) start to emanate from the outer tips of flaws at 282.8 μs . When the rock specimen reaches the peak stress at 322.2 μs , some tensile-shear mixed cracks (TS2 crack) propagate to the transmitted end of rock specimen. Then, the rock specimen enters the post-peak stage, the mixed cracks (TS2 crack and CS2 crack) further propagate and coalesce with specimen ends (366.1 μs) leading the final catastrophic failure of rock specimen.

As can be seen in Fig. 12, most cracks initiate from the edge of prefabricated flaws. A few thresholds of crack propagation locate at the corner of the specimen due to stress concentration. Generally, with the pre-stress ratio fixed at 0.4, the multi-flawed rock specimens failed in mixed cracking mechanism. Under relative lower inclination angles (15° and 30°), a large amount of tensile cracks (DT crack and RT crack) and tensile-shear cracks (TS2 crack) are observed to horizontally propagate on the specimen surface, indicating that the tensile-shear mixed cracking mechanism are dominated among rock specimens with lower flaw inclination angles. However, more mixed cracks (TS2 crack and CS2 crack), especially the compression-shear cracks, are observed to diagonally propagate among rock specimens with relative higher flaw inclination angles (45° and 60°). It is thus can be concluded that the shear cracking mechanism becomes more popular for the rock specimens with higher flaw inclination angles.

3.3.3 Failure Modes

To further understand the comprehensive influences of pre-stress ratio and flaw inclination angle on the cracking behaviors and failure mechanism of multi-flawed rocks under coupled static–dynamic compression loading, Fig. 13 presents the typical failure modes of tested rock specimens with distinct inclination angles under different pre-stress ratios. And the corresponding displacement fields are also presented accompanied with DTLs for facilitating insightful fracture mechanism analysis. In general, under coupled static–dynamic compression loading, the multi-flawed rock specimens failed in “X” or half “X” shaped failure modes. And the failure mechanism is dominated by mixed cracking, especially mixed compression-shear cracking.

It can be clearly found that the flaw inclination angle evidently affects cracking behaviors of multi-flawed rocks as shown in Fig. 13. For the multi-flawed rock specimens with

relative lower inclination angles (15° and 30°), more tensile cracks (e.g., DT crack and RT crack) and tensile-shear cracks (TS2 crack) are observed to coalesce with flaw tips and the specimen ends. With the flaw inclination angles become higher (45° and 60°), more compression-shear cracks (CS1 crack and CS2 crack) and tensile-shear cracks (TS2 crack) are found to originate from the specimen ends and diagonally coalesce with flaw tips. The inner tips of flaws are usually connected by compression-shear or tensile-shear cracks. Therefore, it can be concluded that the failure mechanism of multi-flawed specimens with relative lower flaw inclination angle is dominated by tensile-shear cracking; while the shear cracking becomes more prominent under higher flaw inclination angles, leading to the compression-shear mixed failure mechanism.

The pre-stress ratio also significantly affects the cracking behaviors and failure mechanism of multi-flawed rocks under coupled static–dynamic compression loading. For the specimens with relative lower flaw inclination angles (15° and 30°), the tensile cracking (DT crack and RT crack) decreases while the shear cracking (CS1 crack, CS2 crack, TS1 crack and TS2 crack) increases with the increase of pre-stress ratios, indicating that the pre-stress ratio promotes the shear cracking under lower flaw inclination angles. However, for the rock specimens with high inclination angles (45° and 60°), more tensile cracks (RT crack) and tensile-shear mixed cracks (TS2 crack) can be observed with the increase of pre-stress ratio. Therefore, it is concluded that the pre-stress ratio promotes the tensile cracking under high flaw inclination angles.

3.4 Energy Evolution

Based on the analysis of energy evolution in Sect. 2.4, the energy partitions can be calculated using Eqs. (9), (10). Table 4 summarized the energy partitions of multi-flawed rock specimens in test group A. Figure 14 presents the influences of strain rate and flaw inclination angle on the energy utilization efficiency and the energy dissipation density. From Fig. 14a, it is concluded that the energy utilization efficiency of the multi-flawed rock specimens is between 15 and 55%, and the energy utilization efficiency generally decreases with increasing strain rate regardless flaw inclination angles. In addition, for a given strain rate, the energy utilization efficiency reaches the minimum at flaw inclination angle of 45° and the maximum at 60° . On the contrary, Fig. 14b indicates that increasing strain rate promotes the energy dissipation density. Specifically, with strain rate increasing from ~ 30 to $\sim 150/\text{s}$, the energy dissipation density increases from ~ 0.3 to $\sim 1.5 \text{ J}/\text{cm}^3$. For a given strain rate, the energy dissipation density first decreases then increases with the flaw inclination angle increasing from 15° to 60° , and the minimum is achieved at 45° while the

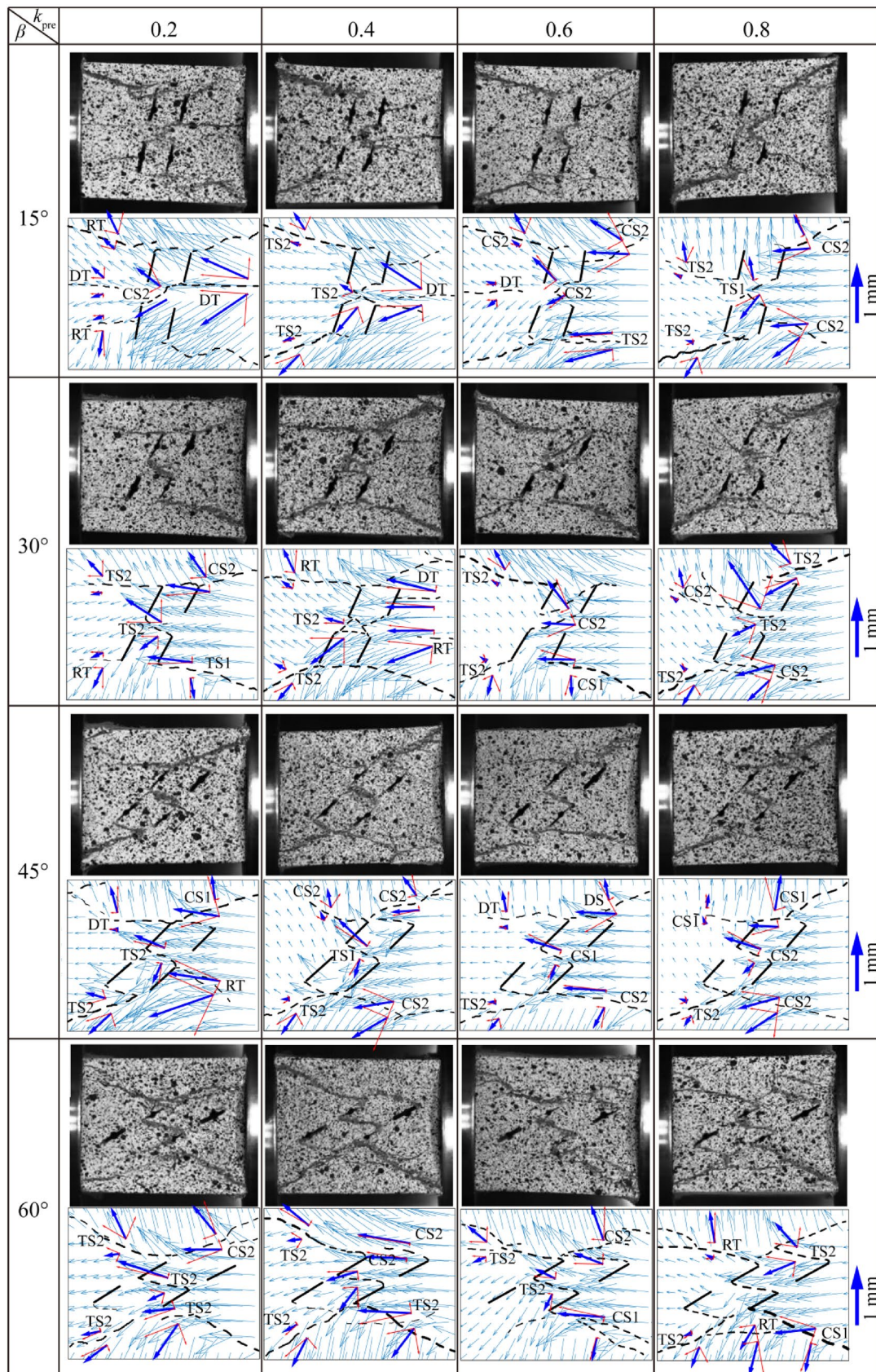


Fig. 13 Comparison of the failure modes of multi-flawed rock specimens with four different inclination angles under distinct pre-stress ratios

Table 4 Energy partitions of multi-flawed rock specimens with different inclination angles under coupled static–dynamic compression with a fixed pre-stress ratio of 0.4

Specimen no	Strain rate (/s)	Incident energy (J)	Reflected energy (J)	Transmitted energy (J)	Absorbed energy (J)
A15-D4-1	32.4	49.0	15.1	12.6	21.4
A15-D4-3	38.8	85.2	35.1	13.1	36.9
A15-D4-5	66.6	87.0	45.2	8.6	33.3
A15-D4-4	81.3	144.5	75.0	12.5	57.0
A15-D4-6	112.9	247.5	160.0	12.2	75.3
A15-D4-2	152.4	286.5	199.9	9.9	76.6
A30-D4-1	31.9	52.1	20.0	12.1	20.0
A30-D4-3	50.9	58.7	25.0	13.3	20.4
A30-D4-4	67.9	75.4	40.1	12.3	23.1
A30-D4-5	103.4	213.4	147.5	9.4	56.5
A30-D4-6	125.3	285.5	214.9	7.5	62.9
A30-D4-2	142.5	306.0	214.4	11.8	79.8
A45-D4-1	43.7	54.2	33.9	8.7	11.5
A45-D4-3	61.3	78.6	49.2	7.9	21.5
A45-D4-2	78.0	137.7	101.1	9.5	27.1
A45-D4-5	91.2	201.6	155.0	9.2	37.5
A45-D4-6	131.0	236.4	179.9	10.4	46.0
A45-D4-4	158.1	282.6	220.0	12.5	50.0
A60-D4-6	21.1	47.7	6.9	15.9	24.8
A60-D4-1	29.9	48.0	8.1	16.9	23.2
A60-D4-3	50.2	85.3	31.1	15.7	38.5
A60-D4-4	70.0	127.7	52.1	13.9	61.6
A60-D4-5	116.1	201.5	109.3	14.2	78.0
A60-D4-2	126.0	285.3	176.0	13.2	96.0

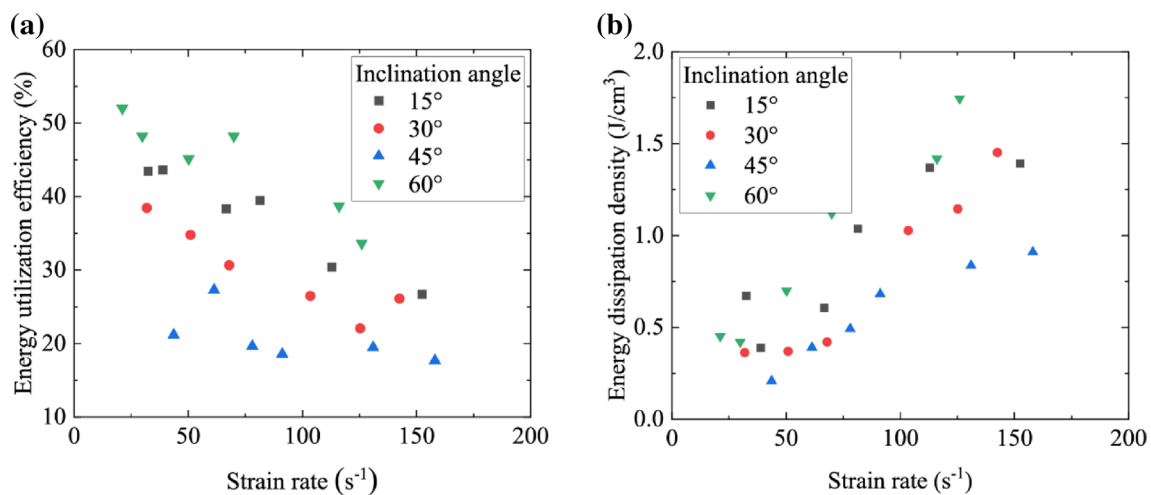


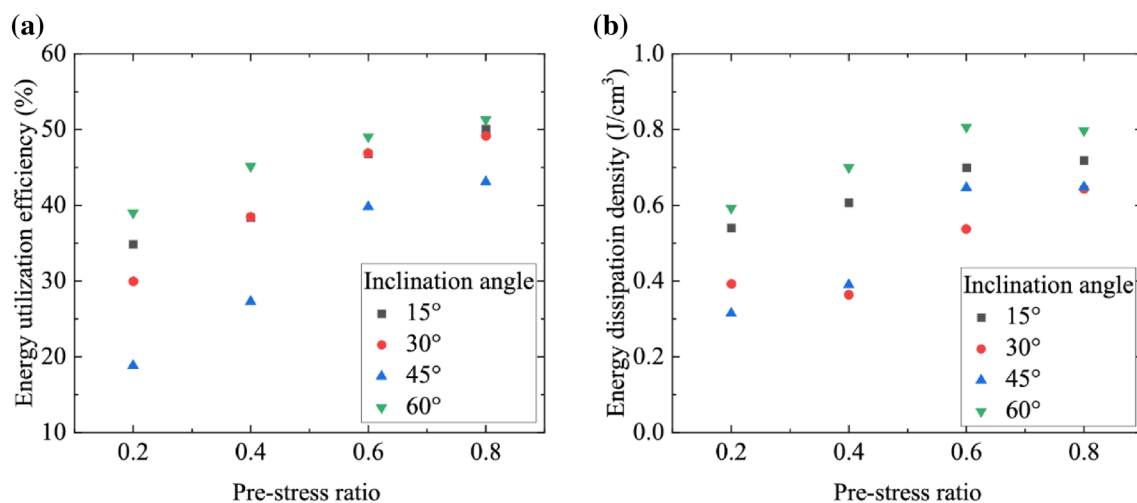
Fig. 14 Influences of strain rate and flaw inclination angle on the energy utilization efficiency and the energy dissipation density with a fixed pre-stress ratio of 0.4

maximum achieved at 60°. This decrease–increase trend is somewhat alike to that of the dynamic/total strength due to the fact that the higher strength means more energy shall be dissipated for rock failure.

Table 5 summarized the energy partitions of multi-flawed rock specimens in the test group B. Figure 15 shows the influences of pre-stress ratio and flaw inclination angle on the energy utilization efficiency and the energy dissipation density. From Fig. 15a, it is evident that the

Table 5 Energy partitions of multi-flawed rock specimens with different inclination angles under different pre-stress ratios with a fixed strain rate at $\sim 45/s$

Specimen no	Pre-stress (MPa)	Incident energy (J)	Reflected energy (J)	Transmitted energy (J)	Absorbed energy (J)
A15-D2-3	7.7	85.2	41.9	13.4	29.7
A15-D4-3	15.4	85.2	35.1	13.1	36.9
A15-D6-3	23.1	82.2	33.3	10.4	38.4
A15-D8-3	30.9	68.0	26.9	6.9	34.0
A30-D2-3	7.6	72.0	38.1	12.4	21.5
A30-D4-3	15.3	58.7	25.0	13.3	20.4
A30-D6-3	23.0	63.1	24.9	8.5	29.5
A30-D8-3	30.6	71.9	28.9	7.7	35.4
A45-D2-3	7.5	92.0	63.3	11.4	17.3
A45-D4-3	15.1	78.6	49.2	7.9	21.5
A45-D6-3	22.7	89.3	42.7	11.0	35.6
A45-D8-3	30.3	82.8	41.7	5.33	35.6
A60-D2-3	7.8	83.6	30.0	20.9	32.6
A60-D4-3	15.7	85.3	31.1	15.7	38.5
A60-D6-3	23.9	90.4	30.6	15.4	44.4
A60-D8-3	31.3	85.5	30.2	11.4	43.9

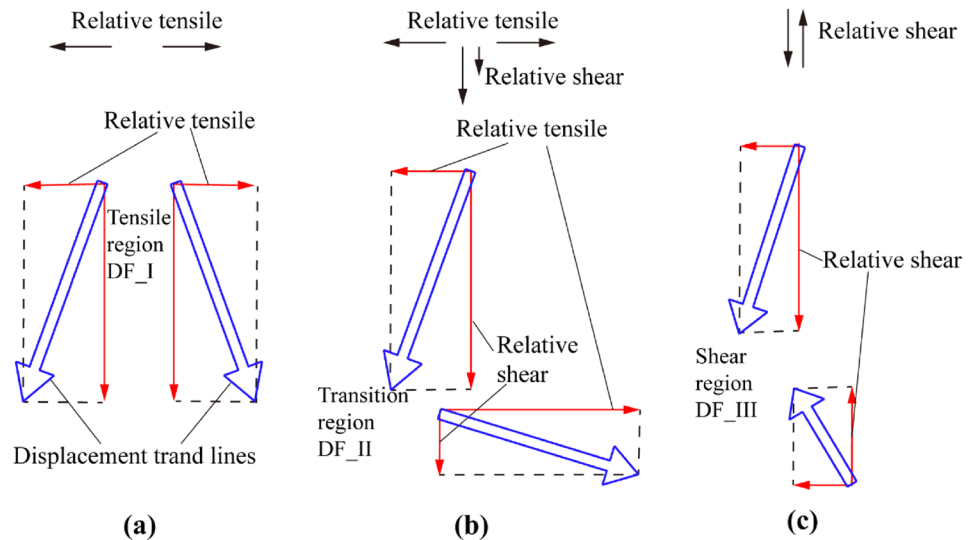
**Fig. 15** Influences of pre-stress ratio and flaw inclination angle on the energy utilization efficiency and the energy dissipation density with the fixed strain rate around $45/s$

energy utilization efficiency increases with increasing of pre-stress ratio from 0.2 to 0.8 regardless flaw inclination angles. For a given pre-stress ratio, the energy utilization efficiency reaches the minimum at flaw inclination angle of 45° and the maximum at 60° . Additionally, the increment at 45° is much larger than that at 60° . The energy dissipation density also increases with increasing pre-stress ratios from 0.2 to 0.8 regardless flaw inclination angles as shown in Fig. 15b. Furthermore, for a given pre-stress ratio, the energy dissipation density also achieves the minimum at flaw inclination angle around 45° and the maximum at 60° .

4 Discussion

In this study, a new crack classification method is proposed to analyze the progressive cracking behaviors of multi-flawed rocks based on high-speed photography and DIC technique. In addition, the energy calculation methods for coupled static–dynamic SHPB tests are re-evaluated and a novel energy calculation formula is proposed to analyze the energy evolution characteristics. Herein, some critical

Fig. 16 Three crack types defined by Zhang and Wong (2014): **a** type I displacement field (DF_I); **b** type II displacement field (DF_II); **c** type III displacement field (DF_III)



issues related to the new crack type classification and the novel energy calculation method are discussed below.

In previous studies by Zhang and Wong (2014), the DTL method was first introduced to identify the cracking mechanism of flawed rock based on DEM simulations, and three crack types were proposed (Fig. 16) based on the observation of some simulation results. As the geometry of fabricated flaws and loading condition become more complex, more new crack types and coalescence patterns may occur in experiments or simulations, which is beyond the scope of existing crack classifications (Zhang and Wong 2013b). With the aid of high-speed photography and DIC technique, the DTL method is further extended to laboratory flawed rock tests. A novel crack classification including eight crack types is thus proposed in this study. In fact, our crack type classification is a new development of previous crack classification by Zhang and Wong (2014). Our crack type classification method is based on distinguishing basic fracture nature of cracks (i.e., tension and shear), and thus, this novel crack type classification is more universal. The existing three crack types (Fig. 16) are included in the new eight crack types: DF_I corresponding to DT crack, DF_II corresponding to TS2 crack and DF_III corresponding to DS crack. The rest five crack types (i.e., RT crack, RS crack, TS1 crack, CS1 crack and CS2 crack) are newly developed. As detailed in Sect. 3.3.1, our crack type classification method is developed based on the quantitative description of the displacement field and DTLs. As long as DIC technique is used during laboratory experiments, for rock specimens with different flaw configurations under different loading conditions, our crack type classification method is reliable and applicable for characterizing the crack fracture mechanism.

To further verify our proposed crack type classification method, the cracking mechanism of a typical single-flawed

45° specimen under dynamic loading is analyzed and compared with previous studies by Zou and Wong (2014). Figure 17a–d shows the horizontal displacement, vertical displacement, maximal principle strain field and macro-crack trajectories near peak stress. It can be found that the anti-wing cracks and coplanar shear cracks dominate the failure and the failure is “X” shaped mixed failure mode. Similar crack propagation and failure pattern also have been observed by Zou and Wong (2014) as show in Fig. 17e. Using the novel crack classification method, these four cracks are identified as TS2 cracks and CS2 cracks (Fig. 17f). Based on the analysis in Sect. 3.3.1, the nature of these two crack types are mixed cracking and thus the failure of the specimen is considered to be dominated by mixed fracture, which is similar to the conclusions by Zou and Wong (2014).

For the traditional SHPB tests, energy partitions related to the three stress waves can be determined by Eq. (12) (Song and Chen 2006; Zhang et al. 2000):

$$\begin{aligned}
 W_i &= K_i + U_i = c_b A_b E_b \int_0^t \varepsilon_i^2 d\tau, \\
 W_r &= K_r + U_r = c_b A_b E_b \int_0^t \varepsilon_r^2 d\tau, \\
 W_t &= K_t + U_t = c_b A_b E_b \int_0^t \varepsilon_t^2 d\tau.
 \end{aligned} \tag{12}$$

Compared with the traditional energy calculation formula (i.e., Eq. 12), the new developed energy calculation formula (i.e., Eq. 8) considers the elastic strain energy caused by the axial pre-stress in the elastic bars. The basic reason for the difference between Eqs. (8) and (12) is that, when calculating the elastic strain energy, the starting point for the integral in Eq. (6) is the pre-strain ε_{pre} rather than 0. It is widely acknowledged that the elastic strain energy is closely

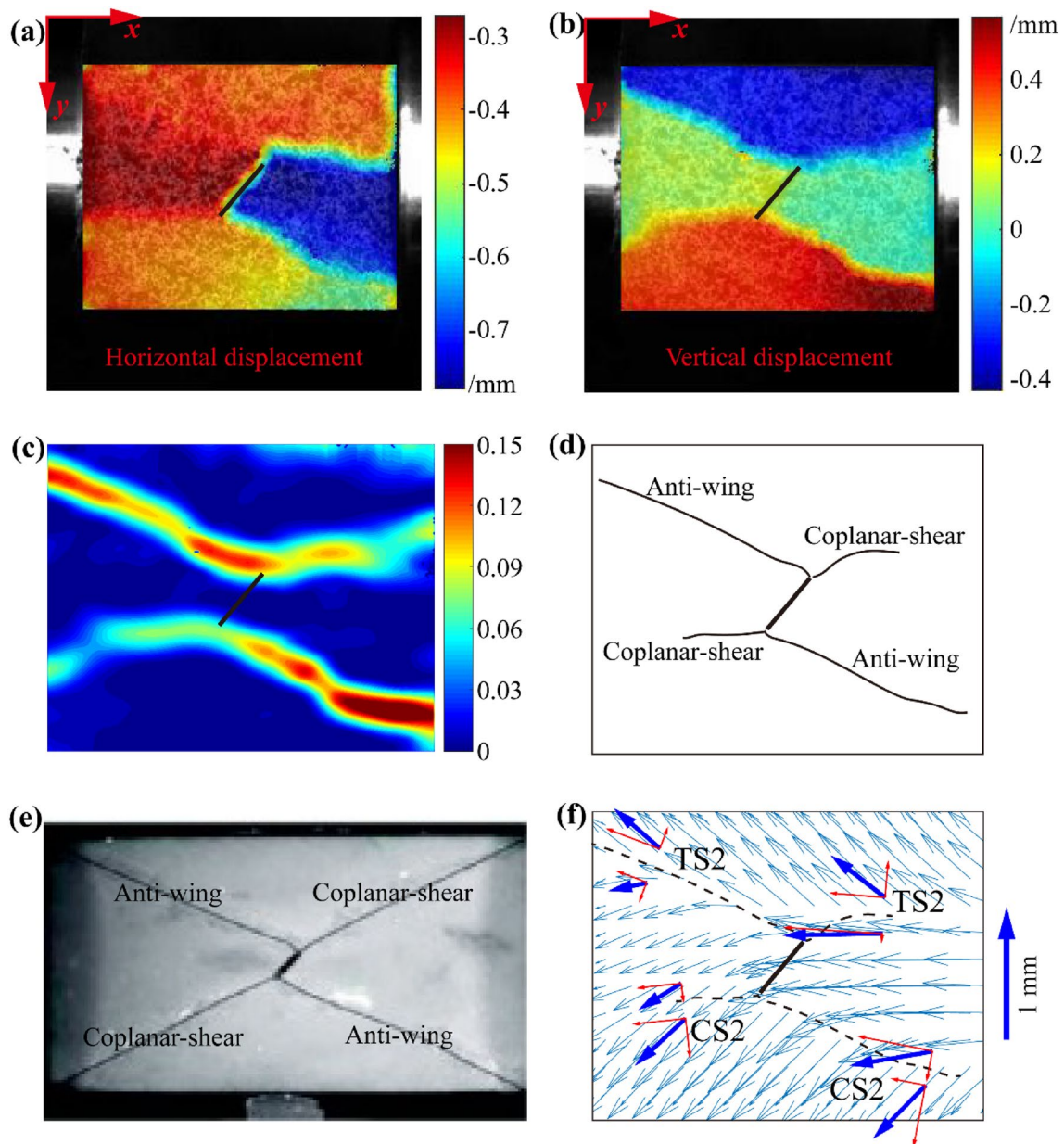


Fig. 17 Validation of the novel crack classification using a 45° single-flawed rock specimen under dynamic loading: **a** horizontal displacement filed; **b** vertical displacement filed; **c** maximal principle strain

filed; **d** macro-crack trajectories; **e** cracking pattern observed by Zou and Wong (2014); **f** new cracking analysis using DTLs method

related to the stress state of materials. Thus, the elastic strain energy in the bars shall be affected by the axial pre-stress in the coupled static–dynamic SHPB tests. Blindly applying the traditional SHPB energy calculation formula to coupled static–dynamic SHPB tests may lead to unreliable results. In this study, the energy values calculated by the new formula are listed in Tables 4 and 5. The absorbed energy increases with increasing incident energy, and this trend is similar to that observed by Zhou et al. (2020a, b). From Tables 4 and 5, it can be clearly found that all the absorbed energy values calculated by the new formula are positive in this

study. However, the absorbed energy values calculated by Zhou et al. (2020a, b) using the traditional formula may be negative under relative high pre-compression stresses. From the viewpoint of energy conservation of rock specimen, it is impossible for the rock specimen to feature negative values of absorbed energy, considering that the failure of rocks is inevitably accompanied with energy consumption. Therefore, the influence of axial pre-compression stress on the energy evolution must be considered in the coupled static–dynamic SHPB tests, otherwise the experimental results may be controversial.

5 Conclusions

In this study, multi-flawed rock specimens with different inclination angles are tested under coupled static–dynamic compression loading using the SHPB system modified with an axial confinement unit. Using high-speed photography and DIC technique, the progressive cracking processes of multi-flawed rock specimens are captured and analyzed. This study highlights the comprehensive effects of flaw inclination angle, pre-stress ratio and strain rate on the dynamic properties of multi-flawed rocks, regarding dynamic strength, progressive cracking behaviors and energy dissipation characteristics, under coupled static–dynamic compression loading. Main conclusions are drawn as follows.

1. The dynamic/total strength of the multi-flawed rocks increases with the increase of strain rate, showing evident rate-dependence. With the flaw inclination angle increasing from 15° to 60° , the dynamic/total strength first decreases then increases with the minimum achieved at inclination angle around 45° . In addition, with the increase of pre-stress ratios from 0.2 to 0.8, the dynamic strength persistently decreases. However, the total strength initially increases and subsequently decreases with the maximum achieved at pre-stress ratio of 0.6.
2. By virtual of high-speed photography and DIC technique, strain fields and displacement fields of rock specimens are visualized. Based on displacement trend lines method, a novel crack type classification method is developed to analyze the progressive cracking behaviors and failure mechanism of multi-flawed rocks under impact loading. This novel crack type classification is proved to be a universal and reliable method to identify the cracking mechanism of different flawed rock specimens under various loading conditions.
3. The pre-stress ratio and flaw inclination angle comprehensively affect the progressive cracking behaviors of multi-flawed rocks. For a given pre-stress ratio, the failure mechanism transforms from tensile-shear cracking dominated to compress-shear cracking dominated with increasing flaw inclination angle from 15° to 60° . With increasing pre-stress ratio from 0.2 to 0.8, the shear cracking become more predominant under lower flaw inclination angles while tensile cracking becomes more prominent under higher flaw inclination angles.
4. Energy evolutions for coupled static–dynamic SHPB tests are re-evaluated and a novel energy calculation formula is proposed to analyze the energy characteristics. For a fixed pre-stress ratio, the increasing strain rate reduces the energy utilization efficiency while promotes the energy dissipation density. For a given strain

rate, both the energy dissipation density and energy utilization efficiency increases with increasing pre-stress ratio. Additionally, all rock specimens feature positive absorbed energy values in the coupled static–dynamic compression tests.

Acknowledgements The authors thank the financial support from the National Natural Science Foundation of China (nos. 52039007 and 51779164) and the Youth Science and Technology Innovation Research Team Fund of Sichuan Province (2020JDTD0001).

References

- Aliabadian Z, Zhao G, Russell AR (2019) Crack development in transversely isotropic sandstone discs subjected to Brazilian tests observed using digital image correlation. *Int J Rock Mech Min* 119:211–221
- Bahaaddini M, Sharrock G, Hebblewhite BK (2013) Numerical investigation of the effect of joint geometrical parameters on the mechanical properties of a non-persistent jointed rock mass under uniaxial compression. *Comput Geotech* 49:206–225
- Bobet A (2000) The initiation of secondary cracks in compression. *Eng Fract Mech* 66(2):187–219
- Bobet A, Einstein HH (1998) Fracture coalescence in rock-type materials under uniaxial and biaxial compression. *Int J Rock Mech Min* 35(7):863–888
- Brace WF, Bombolakis EG (1963) A note on brittle crack growth in compression. *J Geophys Res* 68(12):3709
- Cao R, Cao P, Lin H, Pu C, Ou K (2016) Mechanical behavior of brittle rock-like specimens with pre-existing fissures under uniaxial loading: experimental studies and particle mechanics approach. *Rock Mech Rock Eng* 49(3):763–783
- Chen R, Yao W, Lu F, Xia K (2018) Evaluation of the stress equilibrium condition in axially constrained triaxial SHPB tests. *Exp Mech* 58(3):527–531
- Dai F, Huang S, Xia K, Tan Z (2010) Some fundamental issues in dynamic compression and tension tests of rocks using split Hopkinson pressure bar. *Rock Mech Rock Eng* 43(6):657–666
- Du H, Dai F, Liu Y, Xu Y, Wei M (2020a) Dynamic response and failure mechanism of hydrostatically pressurized rocks subjected to high loading rate impacting. *Soil Dyn Earthq Eng* 129:105927
- Du H, Dai F, Xu Y, Yan Z, Wei M (2020b) Mechanical responses and failure mechanism of hydrostatically pressurized rocks under combined compression-shear impacting. *Int J Mech Sci* 165:105219
- Frew DJ, Forrestal MJ, Chen W (2002) Pulse shaping techniques for testing brittle materials with a split Hopkinson pressure bar. *Proc Soc Exp Mech Inc* 49(1):93–106
- Huang Y, Yang S, Zhao J (2016) Three-dimensional numerical simulation on triaxial failure mechanical behavior of rock-like specimen containing two unparallel fissures. *Rock Mech Rock Eng* 49(12):4711–4729
- Ji WW, Pan PZ, Lin Q, Feng XT, Du MP (2016) Do disk-type specimens generate a mode II fracture without confinement? *Int J Rock Mech Min* 87:48–54
- Jiang RC, Dai F, Liu Y, Li A (2021) Fast marching method for micro-seismic source location in cavern-containing rockmass: performance analysis and engineering application. *Engineering*. <https://doi.org/10.1016/j.eng.2020.10.019>
- Kolsky H (1949) An investigation of the mechanical properties of materials at very high rates of loading. *Proc Phys Soc Sect B* 62(11):676–700

- Lee H, Jeon S (2011) An experimental and numerical study of fracture coalescence in pre-cracked specimens under uniaxial compression. *Int J Solids Struct* 48(6):979–999
- Li X, Zhou Z, Lok T, Hong L, Yin T (2008) Innovative testing technique of rock subjected to coupled static and dynamic loads. *Int J Rock Mech Min* 45(5):739–748
- Li X, Zhou T, Li D (2017) Dynamic strength and fracturing behavior of single-flawed prismatic marble specimens under impact loading with a split-Hopkinson pressure bar. *Rock Mech Rock Eng* 50(1):29–44
- Li D, Han Z, Sun X, Zhou T, Li X (2019) Dynamic mechanical properties and fracturing behavior of marble specimens containing single and double flaws in SHPB tests. *Rock Mech Rock Eng* 52(6):1623–1643
- Li A, Liu Y, Dai F, Liu K, Wei M (2020a) Continuum analysis of the structurally controlled displacements for large-scale underground caverns in bedded rock masses. *Tunn Undergr Sp Tech* 97:103288
- Li D, Gao F, Han Z, Zhu Q (2020b) Experimental evaluation on rock failure mechanism with combined flaws in a connected geometry under coupled static-dynamic loads. *Soil Dyn Earthq Eng* 132:106088
- Lin Q, Yuan H, Biolzi L, Labuz JF (2014) Opening and mixed mode fracture processes in a quasi-brittle material via digital imaging. *Eng Fract Mech* 131:176–193
- Lin Q, Wang S, Pan PZ, Bian X, Lu Y (2020) Imaging opening-mode fracture in sandstone under three-point bending: a direct identification of the fracture process zone and traction-free crack based on cohesive zone model. *Int J Rock Mech Min* 136:104516
- Liu Y, Dai F, Fan P, Xu N, Dong L (2017) Experimental investigation of the influence of joint geometric configurations on the mechanical properties of intermittent jointed rock models under cyclic uniaxial compression. *Rock Mech Rock Eng* 50(6):1453–1471
- Pan B (2018) Digital image correlation for surface deformation measurement: historical developments, recent advances and future goals. *Meas Sci Technol* 29(8):82001
- Pan B, Lu Z, Xie H (2010) Mean intensity gradient: an effective global parameter for quality assessment of the speckle patterns used in digital image correlation. *Opt Laser Eng* 48(4):469–477
- Park CH, Bobet A (2010) Crack initiation, propagation and coalescence from frictional flaws in uniaxial compression. *Eng Fract Mech* 77(14):2727–2748
- Prudencio M, Van Sint JM (2007) Strength and failure modes of rock mass models with non-persistent joints. *Int J Rock Mech Min* 44(6):890–902
- Sagong M, Bobet A (2002) Coalescence of multiple flaws in a rock-model material in uniaxial compression. *Int J Rock Mech Min* 39(2):229–241
- Sharafisafa M, Shen L, Xu Q (2018) Characterisation of mechanical behaviour of 3D printed rock-like material with digital image correlation. *Int J Rock Mech Min* 112:122–138
- Shen B (1995) The mechanism of fracture coalescence in compression experimental study and numerical simulation. *Eng Fract Mech* 51(1):73–85
- Song B, Chen W (2006) Energy for specimen deformation in a split Hopkinson pressure bar experiment. *Exp Mech* 46(3):407–410
- Weng L, Li X, Taheri A, Wu Q, Xie X (2018) Fracture evolution around a cavity in brittle rock under uniaxial compression and coupled static-dynamic loads. *Rock Mech Rock Eng* 51(2):531–545
- Wong RHC, Chau KT (1998) Crack coalescence in a rock-like material containing two cracks. *Int J Rock Mech Min* 35(2):147–164
- Wong LNY, Einstein HH (2009a) Systematic evaluation of cracking behavior in specimens containing single flaws under uniaxial compression. *Int J Rock Mech Min* 46(2):239–249
- Wong LNY, Einstein HH (2009b) Crack coalescence in molded gypsum and carrara marble: part I. Macroscopic observations and interpretation. *Rock Mech Rock Eng* 42(3):475–511
- Xia K, Yao W (2015) Dynamic rock tests using split Hopkinson (Kolsky) bar system—a review. *J Rock Mech Geotech* 7(1):27–59
- Xie H, Zhu J, Zhou T, Zhang K, Zhou C (2020) Conceptualization and preliminary study of engineering disturbed rock dynamics. *Geomech Geophys Geo-Energ Geo-Resour* 6:34
- Xing HZ, Zhang QB, Ruan D, Dehkhoda S, Lu GX, Zhao J (2018) Full-field measurement and fracture characterisations of rocks under dynamic loads using high-speed three-dimensional digital image correlation. *Int J Impact Eng* 113:61–72
- Xu Y, Dai F (2018) Dynamic response and failure mechanism of brittle rocks under combined compression-shear loading experiments. *Rock Mech Rock Eng* 51(3):747–764
- Xu Y, Dai F, Du H (2020) Experimental and numerical studies on compression-shear behaviors of brittle rocks subjected to combined static-dynamic loading. *Int J Mech Sci* 175:105520
- Yan Z, Dai F, Liu Y, Feng P (2019) Experimental and numerical investigation on the mechanical properties and progressive failure mechanism of intermittent multi-jointed rock models under uniaxial compression. *Arab J Geosci* 12:618
- Yan Z, Dai F, Liu Y, Du H, Luo J (2020) Dynamic strength and cracking behaviors of single-flawed rock subjected to coupled static-dynamic compression. *Rock Mech Rock Eng* 53(9):4289–4298
- Zhang X, Wong LNY (2013a) Loading rate effects on cracking behavior of flaw-contained specimens under uniaxial compression. *Int J Fracture* 180(1):93–110
- Zhang X, Wong LNY (2013b) Crack initiation, propagation and coalescence in rock-like material containing two flaws: a numerical study based on bonded-particle model approach. *Rock Mech Rock Eng* 46(5):1001–1021
- Zhang X, Wong LNY (2014) Displacement field analysis for cracking processes in bonded-particle model. *B Eng Geol Environ* 73(1):13–21
- Zhang QB, Zhao J (2014) A review of dynamic experimental techniques and mechanical behaviour of rock materials. *Rock Mech Rock Eng* 47(4):1411–1478
- Zhang ZX, Kou SQ, Jiang LG, Lindqvist PA (2000) Effects of loading rate on rock fracture: fracture characteristics and energy partitioning. *Int J Rock Mech Min* 37(5):745–762
- Zhou T, Zhu JB, Ju Y, Xie HP (2019) Volumetric fracturing behavior of 3D printed artificial rocks containing single and double 3D internal flaws under static uniaxial compression. *Eng Fract Mech* 205:190–204
- Zhou T, Zhu JB, Xie H (2020a) Mechanical and volumetric fracturing behaviour of three-dimensional printing rock-like samples under dynamic loading. *Rock Mech Rock Eng* 53(6):2855–2864
- Zhou Z, Cai X, Li X, Cao W, Du X (2020b) Dynamic response and energy evolution of sandstone under coupled static-dynamic compression: insights from experimental study into deep rock engineering applications. *Rock Mech Rock Eng* 53(3):1305–1331
- Zou C, Wong LNY (2014) Experimental studies on cracking processes and failure in marble under dynamic loading. *Eng Geol* 173:19–31
- Zou C, Wong LNY (2016) Size and geometry effects on the mechanical properties of carrara marble under dynamic loadings. *Rock Mech Rock Eng* 49(5):1695–1708
- Zou C, Wong LNY, Loo JJ, Gan BS (2016) Different mechanical and cracking behaviors of single-flawed brittle gypsum specimens under dynamic and quasi-static loadings. *Eng Geol* 201:71–84